Neural spiking signatures predict behavioral phenotypes of cerebellar movement disorders

Meike E. van der Heijden[1,5,*], Amanda M. Brown[1,5,*], Dominic J. Kizek[5], Roy V. Sillitoe[1-5]

[1]Department of Pathology & Immunology, Baylor College of Medicine, Houston, Texas, USA
[2]Department of Neuroscience, Baylor College of Medicine, Houston, Texas, USA
[3]Department of Pediatrics, Baylor College of Medicine, Houston, Texas, USA
[4]Development, Disease Models & Therapeutics Graduate Program, Baylor College of Medicine, Houston, Texas, USA
[5]Jan and Dan Duncan Neurological Research Institute at Texas Children's Hospital, Houston, Texas, 77030, USA

*These authors contributed equally

Address correspondence to:
Dr. Roy V. Sillitoe
Tel: 832-824-8913
Fax: 832-825-1251
Email: sillitoe@bcm.edu

Dr. Meike E. van der Heijden
Email: meheijde@bcm.edu

Abstract
The cerebellum contributes to a diverse array of motor conditions including ataxia, dystonia, and tremor. The neural substrates that encode this diversity are unclear. Here, we tested whether the neural spike activity of cerebellar output neurons predicts the phenotypic presentation of cerebellar pathophysiology. Using *in vivo* awake recordings as input data, we trained a supervised classifier model to differentiate the spike parameters between mouse models for ataxia, dystonia, and tremor. The classifier model correctly predicted mouse phenotypes based on single neuron signatures. Spike signatures were shared across etiologically distinct but phenotypically similar disease models. Mimicking these pathophysiological spike signatures with optogenetics induced the predicted motor impairments in otherwise healthy mice. These data show that distinct spike signatures promote the behavioral presentation of cerebellar diseases.

Key words
Cerebellum, ataxia, dystonia, tremor, spike train activity, optogenetics, classifier model

Introduction

There exists a historical and rich curiosity in understanding the role of the cerebellum in movement, dating back to the pioneering work of Flourens (1), with an equally long interest in investigating how it alters movement (2, 3). From these earlier studies it was clear that a defective cerebellum causes a range of devastating problems in the ability to control voluntary, intentional actions including coordination, posture, and balance. Accordingly, in humans, the equivalent defects had clear pathophysiological consequences. Patients with various cerebellar lesions showed loss of precise motor coordination, which, as the consequence of disease, is referred to as ataxia, whereas some subjects displayed overt and sometimes exaggerated oscillatory movements, consistent with tremor (2–4). In other cases, the examiner would report uncontrolled muscle contractions, which is now a contributing feature of dystonia (5). These classic observations underscored the heterogeneity of motor disturbances caused by cerebellar dysfunction. But, even then, the question of how the cerebellum creates such behavioral diversity was already imminent. Despite major advances in understanding the basic anatomy and circuitry of the cerebellum, it is still unclear how disease behaviors emerge of these circuits. In this regard, the specific substrates that underlie each disorder could hold the key for improving the design of therapies and treatments.

Consistent with the outcomes of removing or lesioning the cerebellum in pigeons, dogs, monkeys, and humans (2–4), the heterogeneity of cerebellar movement disturbances was later confirmed in genetic mouse models. Much of the current excitement about the cerebellum spawned from these initial genetic models because of the overt motor disturbances that were caused by spontaneous mutations in genes that are now known to be associated with cerebellar development or cerebellar degeneration (6, 7). Prior to genetic sequencing though, mutant mice such as *hot-foot* (8), *weaver* (9), *trembler* (6), *waddles* (10), *staggerer* (11), *stumbler* (12), *tottering* (13), and *lurcher* (14) were named according to phenotype of their abnormal movements, which are as diverse as their names imply. Modern techniques and approaches now aim at determining the mechanisms and roles of the cerebellum as they relate to driving different behaviors in these classic models (15, 16). Together, data generated from these different mouse models have cultivated an interest in identifying whether discrete functional features in the cerebellar circuit are the root cause of disease-related behaviors. In this regard, more than half a century since the first descriptions of cerebellar mutants, a core question remains unanswered but hotly debated: how does cerebellar circuit dysfunction lead to unique motor disturbances?

To begin addressing how cerebellar circuits generate behavioral diversity in disease, we used an intersectional genetics approach to mark, map, and manipulate specific types of synapses in the cerebellum. Our approach silences genetically defined populations of synapses by selectively deleting the genes that encode the vesicular GABA transporter, *Vgat*, or the type 2 vesicular glutamate transporter, *Vglut2*, from genetically targeted populations of cells. Loss of GABAergic neurotransmission from Purkinje cells, which provide the sole output of the cerebellar cortex, caused uncoordinated movements and disequilibrium that were indicative of ataxia (Figure 1A) (17). In contrast, eliminating glutamatergic neurotransmission from climbing fibers, which synapse onto Purkinje cells, caused twisting postures and hyperextended limbs that is consistent with dystonia (Figure 1A) (18). In addition, systemic injection of the beta-carboline alkaloid drug harmaline caused hyperactivation of climbing fibers and rhythmic bursting spike activity in Purkinje cells as well as a severe tremor. Optogenetically modulating Purkinje cell to cerebellar nuclei projections in a bursting pattern induced oscillatory tremor movements (Figure 1A) (19, 20). Together, these studies established that different manipulations of Purkinje cell inputs or outputs, and consequently Purkinje cell and nuclei neuron spike signals, can cause diverse behavioral deficits as they relate to disease (18, 20). Given the heterogeneity and even comorbidity of these behaviors in a single disease model (21), the main question that arises is, do these cerebellar neural signals represent unique pathophysiological signatures that can drive the predominant behavioral defects used to characterize different motor diseases? Here, we aim to resolve this question to provide insight into the origin of cerebellar movement disorder presentation.

Results

Spike signatures are different between archetypal ataxia, dystonia, and tremor models

We first compared the spike train activity between mouse models for ataxia (*L7*^{Cre}*;Vgat*$^{fl/fl}$, (17, 20)), dystonia (*Ptf1a*$^{Cre/+}$*;Vglut2*$^{fl/fl}$, (18, 22)), and tremor (harmaline injection, (20, 23)) (Figure 1A). We identified these three mouse models as archetypal representations of their respective cerebellar motor disease phenotypes because their overt behavioral motor abnormalities are caused by cerebellum-specific manipulations that do not cause changes in the gross anatomy, cell morphology, or cell survival of the adult cerebellum. These models also exhibit remarkably reliable, severe, and penetrant ataxic, dystonic, and tremor symptoms within each respective group. Video 1 provides examples of the varied and overt motor abnormalities of the mouse models used. Supplemental table 1 summarizes the reported behavioral impairments from prior characterization of these archetypal mouse models.

We hypothesized that these differences in behavioral abnormalities were accompanied by specific changes in the spike train patterns in the cerebellum. We performed *in vivo* electrophysiology recordings of the spike activity in cerebellar nuclei neurons of the interposed nucleus (Figure 1B,C), in awake, head-fixed mice with overt motor phenotypes and control animals. We focused our recordings on the interposed nucleus based on the hypothesis that the cerebellum communicates ongoing motor signals to other brain regions through this nucleus (24) and deep brain stimulation (DBS) of this region successfully reduces motor impairments in mouse models of ataxia (25), dystonia (18), and tremor (20). We described the spike train firing features using twelve parameters that summarized the spike train rate (Supp. Figure 1A-C), irregularity (Supp. Figure 1D-F), pauses (Supp. Figure 1G-I), and rhythmicity (Supp. Figure 1J-L). In agreement with our hypothesis, we found a significant difference between at least two archetypal groups for each of the twelve spike train parameters. However, none of the twelve parameters showed a statistical difference between all four groups (control, ataxia, dystonia, and tremor), suggesting that the difference between spike train signatures relied on a combination of multiple spike train parameters.

We therefore set out to find a set of parameters and specific threshold values that best differentiated the spike train parameters between the archetypal groups. We trained a supervised classification learning model based on the spike train parameters of each mouse model (Supp. Figure 1A-L). The classifier model identified the coefficient of variance (CV, Supp. Figure 1D) of interspike intervals (ISI) as the best differentiator of neurons recorded in ataxic and control mice (lower CV) from neurons recorded in dystonic and tremoring mice (higher CV). CV is a measure of variability that increases due to pauses between spikes or fluctuations in the firing rate (Figure 1B) and is unusually elevated in our dystonic and tremor mouse models (Figure 1B”). Next, the classifier model identified CV2 (26) (Supp. Figure 1E) as the best differentiator of neurons recorded in ataxic mice (lower CV2) from control mice (higher CV2). CV2 measures the irregularity of interspike intervals with less influence from the overall firing rate. It is extraordinarily low in the highly regular spike activity observed in our ataxia model (Figure 1B’’). Last, the classifier model identified that the median ISI^{-1} (Supp. Figure 1C), which measures the median instantaneous firing rate, as the best differentiator of neurons from the dystonic mice (lower median ISI^{-1}) compared to those recorded in mice with tremor (higher median ISI^{-1}) (Figure 1C). These findings suggest that changes in a combination of three parameters (CV, CV2, and median ISI^{-1}) may explain the difference in the behavioral presentation of mouse models of cerebellar disease.

We then validated whether this classifier model could reliably predict the behavioral phenotypes of the archetypal mouse models based solely on the spiking activity of single cerebellar nuclei neurons. We tested this by predicting the behavioral phenotype based on CV, CV2, and median ISI^{-1} values calculated based on a different set of recordings. We found that the classifier model indeed predicted the different predominant phenotypes of each archetypal mouse model correctly for the majority of neurons in the validation data set (control: 80% of neurons recorded in a control mouse had a control signature; ataxia: 78%; dystonia: 65%; tremor: 56%) (Figure 1E). Our analyses also showed that most neurons of a specific signature were recorded from the mouse model with that phenotype (control: 59% of neurons

with a control signature were recorded in a control mouse; ataxia: 89%; dystonia: 65%; tremor: 73%) (Figure 1E-G). These data support the hypothesis that spike signatures are reliably different between archetypal mouse models of distinct motor behaviors that mimic human disease symptoms.

Multiple spike train signatures can lead to ataxic motor impairments

Next, we set out to identify whether the spike train signatures for the archetypal mouse models are shared across mouse models with different manipulations but similar phenotypes. We started by classifying the spike train parameters in a mouse model of ataxia caused by a poly-glutamate expansion in the Atxn1 gene, *Atxn1*$^{154Q/+}$ mice, that causes spinocerebellar ataxia type 1 (SCA1). We measured the spike train patterns early in the disease progression (27) (Figure 2A-B). Despite the presence of an ataxic phenotype at this age (Supp. Table 1), we observed that most *Atxn1*$^{154Q/+}$ neurons exhibited a control signature (14/24) and that the second most numerous spike train signature was a dystonia signature (8/24).

We reasoned that the high proportion of cells exhibiting a control signature in *Atxn1*$^{154Q/+}$ mice might be because the disease-causing genetic abnormality affects the whole body and, consequently, the ataxic symptoms may result from dysfunction in multiple nodes in the motor circuit. We therefore also investigated a mouse model with a cerebellum-specific loss of the gene *Ank1* (10-12 month old *L7*^{Cre}*;Ank1*$^{fl/fl}$ mice, Figure 2A), which causes an adult-onset degenerative ataxia (28). In this mouse model, we found that more than half of the neurons exhibited an abnormal spike train signature, with the majority classified with the dystonia spike train signature (7/14).

Our classifier model differentiates the control and dystonia signatures from each other based on the CV parameter. Previous studies have suggested that the difference between ataxia and dystonia symptoms may be caused by the relative difference in CV value (15, 29, 30). Indeed, the distribution of CV values appeared to be lower in the ataxic *Atxn1*$^{154Q/+}$ (0.59 $\pm$ 0.04 (mean $\pm$ SEM)) and *L7*^{Cre}*;Ank1*$^{fl/fl}$ (0.61 $\pm$ 0.07) mouse models (Figure 2D-E) than in our archetypal dystonia model (1.15 $\pm$ 0.11) (*Ptf1a*$^{Cre/+}$*;Vglut2*$^{fl/fl}$, Figure 1F-G). We used a one-way ANOVA followed by a Tukey post-hoc analyses and found that the difference in CV between the ataxia models and the dystonia models was statistically significant (*Atxn1*$^{154Q/+}$ vs. *Ptf1a*$^{Cre/+}$*;Vglut2*$^{fl/fl}$: $p<0.0001$; *L7*^{Cre}*;Ank1*$^{fl/fl}$ vs. *Ptf1a*$^{Cre/+}$*;Vglut2*$^{fl/fl}$: $p<0.0001$), but we did not observe a difference in CV between the two ataxia models (*Atxn1*$^{154Q/+}$ vs *L7*^{Cre}*;Ank1*$^{fl/fl}$: $p=0.9739$). Together, these findings suggest that there are multiple cerebellar spike train signatures that can lead to ataxic symptoms that both differ from the dystonia signature in their relative level of regularity; unusually regular spike train patterns are seen in *L7*^{Cre}*;Vgat*$^{fl/fl}$ mice (Figure 1) and intermediate irregular spike train patterns are observed in *Atxn1*$^{154Q/+}$ and *L7*^{Cre}*;Ank1*$^{fl/fl}$ mouse models (Figure 2).

Dystonic spike train signatures are shared across etiologically distinct dystonia models

Next, we set out to identify whether the dystonia signature was shared across mice with overt dystonic phenotypes. We included two dystonia models in our analyses; *Pdx1*^{Cre}*;Vglut2*$^{fl/fl}$ mice exhibit mild dystonic symptoms only in response to a stressful event (31, 32) (Figure 3A-B), whereas mice that receive ouabain applied to the surface of the cerebellum exhibit continuous severe dystonic features (33, 34) (Figure 3A-B). We found that the proportion of neurons that exhibited the control signature was greater in *Pdx1*^{Cre}*;Vglut2*$^{fl/fl}$ mice than in ouabain infusion mice (11/21 vs. 7/20) (Figure 3C). Moreover, the proportion of neurons with a dystonia signature was lower in *Pdx1*^{Cre}*;Vglut2*$^{fl/fl}$ mice than in ouabain infusion mice (9/21 vs. 11/20) (Figure 3C). Therefore, the mice with a more severe dystonia phenotype had a smaller proportion of cells matching the control signature and a greater proportion of cells matching the dystonia signature. In addition to the proportional differences in cells with a control and dystonia signature, we found that the distribution of CV values differed between the *Pdx1*^{Cre}*;Vglut2*$^{fl/fl}$ (0.61 $\pm$ 0.07) and ouabain infusion mice (1.00 $\pm$ 0.15) (Figure 3D-E). We quantified this difference by comparing these two mouse models to each other and the archetypal dystonic model (*Ptf1a*$^{Cre/+}$*;Vglut2*$^{fl/fl}$) using a one-way ANOVA followed by a Tukey post-hoc analysis. We found that the CV was lower in *Pdx1*^{Cre}*;Vglut2*$^{fl/fl}$ mice

with mild dystonic features compared to the ouabain infusion mice (p=0.0482) and *Ptf1a*$^{Cre/+}$*;Vglut2*$^{fl/fl}$ mice (p=0.0037) with severe dystonic features. There was no significant difference between the two models with severe dystonic features (p=0.5940). These findings show that the dystonia signature is shared across etiologically distinct dystonia models and that the relative severity of symptoms may be explained by the proportion of neurons with a dystonia and control signature (Figure 3).

Tremor spike train signatures are shared across etiologically distinct tremor models

Next, we set out to identify whether the tremor signature is shared across mice that exhibit severe oscillatory tremors. To test this, we used *Car8*$^{wdl/wdl}$ mice. We previously showed that *Car8*$^{wdl/wdl}$ mice exhibit a severe oscillatory tremor that can be reduced to control levels by treatment with the beta blocker drug propranolol (35), which is used to treat tremor in human patients. *Car8*$^{wdl/wdl}$ mice also exhibit ataxia and dystonia, which are not normalized by propranolol (10, 21, 25, 35). We found that, before treatment, *Car8*$^{wdl/wdl}$ mice exhibited a large proportion of neurons with the tremor signature (12/19). However, in propranolol-treated *Car8*$^{wdl/wdl}$ mice the proportion of neurons with the tremor signature was diminished while control (6/15) and dystonia (6/15) signatures were the most common signatures (Figure 4C). The classifier model differentiates between the dystonia and tremor signature based on the median ISI^{-1} value and, indeed, we find a shift towards lower median ISI^{-1} values in propranolol-treated *Car8*$^{wdl/wdl}$ mice compared to untreated *Car8*$^{wdl/wdl}$ mice (Figure 4D-E). Together, these findings suggest that the tremor signature is shared across etiologically distinct mouse models of tremor and that the tremor-reducing drug propranolol also reduces specific spike train features contributing to the tremor signature (Figure 4).

Different spike signatures can be generated by the same canonical cerebellar circuit

Next, we investigated whether the different spike signatures could be generated by the same canonical cerebellar circuit. We reasoned that the observed spike train signatures were not dependent on developmental changes in circuit connectivity (*L7*^{Cre}*;Vgat*$^{fl/fl}$; *Ptf1a*$^{Cre/+}$*;Vglut2*$^{fl/fl}$; *Pdx1*^{Cre}*;Vglut2*$^{fl/fl}$), neurodegeneration (*Atxn1*$^{154Q/+}$*; L7*^{Cre}*;Ank1*$^{fl/fl}$), the effects of transgene expression (*Atxn1*$^{154Q/+}$) or frameshifting (*Car8*$^{wdl/wdl}$), or drug effects on the nervous system outside of the cerebellum (harmaline, ouabain, propranolol). We expressed a light-sensitive cation channel opsin, channelrhodopsin (ChR2), in Purkinje cells (*L7*^{Cre}*;ROSA26*$^{loxP\text{-}STOP\text{-}loxP\text{-}EYFP\text{-}ChR2}$ mice, hereon referred to as *L7*^{Cre}*;R26*^{ChR2} mice). Upon light activation, Purkinje cell firing rate increases (Supplemental Figure 2A-B) and nuclei neurons are inhibited via the GABAergic neurotransmission from Purkinje cells (Figure 5A-C). We leveraged this circuit connectivity and optogenetic strategy to induce distinct spike signatures in cerebellar neurons. We chose three stimulation paradigms. The ataxia stimulation was a continuous 50 Hz square pulse stimulation (mimicking the lack of modulation by Purkinje cells in our degenerative and genetically silenced ataxia models); the dystonia stimulation was a 50 Hz square pulse stimulation that was on for at least 500 ms with a 75% chance of a 250 ms pause between periods of stimulation (to induce the slow and irregular spike train features of our defined dystonia signature); and the tremor stimulation was a 10 Hz sinusoidal stimulation (to induce the fast, irregular, and rhythmic spike train features of our defined tremor signature). We performed *in vivo* recordings in awake, head-fixed mice, and confirmed that each of the optogenetic stimulation paradigms caused distinct changes in Purkinje cell spiking activity (Supplemental Figure 2). The different stimulation paradigms also induced distinct changes in the spike train features of cerebellar nuclei neurons (Figure 5D). We then compared the resultant spike train features to the defined thresholds of our classifier model. We found that the ataxia stimulation paradigm induced cells to behave within the parameters of a variety of our defined spike train signatures, including ataxia (2/9), dystonia (2/9), and tremor (2/9). This is in line with our findings that the ataxia signature is more variable across ataxia mouse models (Figure 2). Importantly, we found that fewer than half of the cells recorded with the ataxia stimulation exhibited a control signature (Figure 5F), similar to the proportional distribution of cells in other mouse models with severe motor phenotypes (Figure 2C, 3C, 4C). Additionally, we found that the dystonia and tremor stimulation reliably induced spike signatures that our classifier model defined as dystonic (7/7 cells) or as tremor signatures (9/9 cells), respectively (Figure 5F). These data indicate that no anatomical changes are required to induce disease-associated spike

signatures in the cerebellum and that spike signatures associated with ataxia, dystonia, and tremor can be generated by the same, otherwise healthy, cerebellar circuit.

Spike signatures can induce distinct motor phenotypes that mimic disease-related behaviors

During the head-fixed stimulation experiments, we observed subtle behavioral responses during unilateral cell-targeted optogenetic stimulation that suggested the different spike signatures might drive unique motor behaviors (Video 2). To explore this further in freely moving mice, we investigated whether the different spike signatures directly drive unique motor disturbances when a population of cells are induced to produce our defined spike signatures. To this end, $L7^{Cre};R26^{ChR2}$ mice were implanted with optical fibers that were bilaterally targeted to the interposed cerebellar nuclei (Figure 6A-C). This allowed for the targeting of Purkinje cell terminals in the cerebellar nuclei, as was done during our *in vivo* recordings in Figure 5, but with a larger population of cells affected by the stimulation. This also allowed the mice to move freely during stimulation, making a series of behavioral assays during stimulation possible (Figure 6D). Changes in behavior were immediate and severe as soon as the stimulation began. Each stimulation paradigm resulted in a different constellation of behaviors with the ataxia stimulation paradigm resulting in imprecise movements, the dystonia stimulation paradigm resulting in prominent dystonic posturing, and the tremor stimulation paradigm resulting in severe tremor (Video 3). Therefore, we assessed the mice for changes in gait, presence of dystonic movements, and severity of tremor. No single measurement can perfectly encapsulate the complexity of ataxia, dystonia, and tremor – all of which can appear in combination with the others (36–38). Additionally, each phenotype may affect the measurement of others. This was particularly apparent with measurements of gait. We found that all stimulation paradigms affected gait, resulting in visibly different foot placement (Figure 6E-F) and movement down the footprinting corridor (Video 4). Quantitatively, this was evident in shorter steps and less precision of fore and hindpaw placement (Figure 6I-K). We also considered the behavior of the mice in an open, flat, plexiglass arena for signs of dystonic movements (Figure 6L, Video 3). The dystonia stimulation paradigm resulted in the most frequent and strongest dystonic movements, while we also observed dystonic movements with the ataxia paradigm and abnormal movement – namely severe tremor – was noted with the tremor stimulation paradigm (Figure 6M). Mice were also placed in a custom-made tremor monitor (20) where they could freely ambulate during stimulation while an accelerometer mounted under the arena detected changes in acceleration (Figure 6D). While the ataxia stimulation paradigm did not significantly increase tremor from baseline, both the dystonia and tremor stimulation paradigms resulted in a significantly increased tremor at 10 Hz (Figure 6N-P). Though dystonia is often observed with tremor, it is possible that the detection of tremor in these animals was due to the jerkiness of their dystonic movements rather than an increase in smooth, rhythmic tremor that is more often associated with tremor disorders. Indeed, the tremor paradigm resulted in the most severe tremor of all stimulation conditions, producing a tremor severity that was more than ten-fold greater than that of the dystonia stimulation paradigm. Together, these measurements produced a complex representation of the underlying phenotypes. All three stimulation parameters resulted in a behavioral repertoire that was significantly different from baseline and, while there was some overlap of features, each stimulation paradigm produced the distinct and predicted respective motor phenotype (Figure 6Q-T). Together these data suggest that our classifier model's defined spike signatures of disease-associated cerebellar nuclei spike trains are sufficient to produce the predicted corresponding abnormal motor phenotypes in mice.

Discussion

In this study, we tested whether distinct spike train signatures in the interposed cerebellar nuclei explain why cerebellar dysfunction can cause multiple distinct motor impairments associated with movement disorders. By comparing spike activity across multiple mouse models of cerebellar disease, we found that the cerebellum can generate a range of dysfunctional spiking patterns. We found disease-specific spike train signatures using a classifier learner model, which allowed us to discover specific spike train parameters and their corresponding cutoff values that could distinguish the activity associated with these different disease states. When investigating whether these spike signatures are shared across mouse models with similar phenotypes due to different etiologies, we found that two types of spike train activity can cause ataxia, whereas specific spike train signatures are strongly associated with dystonia and tremor. We then tested whether we could optogenetically induce these signatures in an otherwise normal circuit. We found that the same neurons can generate healthy spike activity as well as a spectrum of disease-like spike activities. We then tested whether these optogenetically-induced disease-associated spike signatures could elicit similar behavioral abnormalities in the absence of any other primary genetic or circuit defects in awake and freely moving mice. The predominant behaviors that characterize each disease condition were successfully recapitulated. These data provide compelling evidence for the reliance of neurological phenotype presentation on the pattern of cerebellar circuit misfiring.

Several previous studies have proposed that distinct spike train patterns may correspond to distinct presentations of cerebellar disease (15, 29, 30, 39). Our work builds on these studies by quantitatively comparing spike train properties across, rather than within, mouse models. We demonstrate what aspects of the spike train patterns are distinct and shared across mouse models with different and similar disease phenotypes, respectively. We confirm prior research indicating the importance of spike train irregularity in disease presentation (15, 29, 39). We also show that spike train irregularity is insufficient to differentiate the spike train properties of dystonic and tremoring mice, which are differentiated from each other based on the instantaneous spike rate rather than pattern. Additionally, we confirm that the spike train signatures associated with different disorders can cause distinct disease phenotypes, thereby showing for the first time that distinct cerebellar spike train signatures are sufficient to drive a variety of motor impairments. Together, these data provide strong evidence that different spike train signatures do not only result from sensory feedback towards the cerebellum and that they may be a primary cause for motor impairments associated with cerebellar disease.

Our work suggests that there is a healthy range within the characteristics of cerebellar nuclei spiking activity and that cerebellar movement disorders are associated with a shift from this range in one or multiple features of spike train activity. We find some overlap and shared spike features between the different disease phenotypes and show that healthy cerebellar neurons can adapt multiple disease-associated spike train signatures. These findings suggest that pathophysiological spike train signatures are driven by a shift in neural function towards a disease state that can be independent of plasticity or circuit rewiring. Despite the dramatically different behavioral outcomes, the potential overlap and shared spike features, such as the irregular spike pattern found in the dystonia and tremor signatures, raise the strong possibility that co-expression or comorbidity of different motor disease behaviors may arise due to a spectrum of spike signal defects. This indicates that it is possible for neural signals to shift back and forth between healthy and disease states, potentially resulting in the transientness of behavioral impairments in certain cerebellar disorders. These findings also suggest that the most successful therapeutic avenues for cerebellar movement disorders should maintain cerebellar spiking activity within the healthy range without inadvertently inducing a different pathophysiological signature.

There has been (40), and there still remains (41), a great interest in understanding how altered cerebellar signals influence human behavior and disease. A pressing need to better define the architecture of these spiking abnomalities has arisen because of the success in using deep brain stimulation (DBS) and the potential for better tuning of the stimulation parameters for greater efficacy in

treating different cerebellar-related disorders (ataxia: (42, 43); dystonia: (44); tremor: (45, 46); ataxia, dystonia, tremor: (41)). Recordings in human patients during DBS implantation have previously found physiological differences in the spike train patterns of basal ganglia neurons between dystonia and other movement disorders (for example; etiologically distinct dystonia: (47); dystonia with and without head tremor: (48); dystonia versus Parkinson's disease: (49)). Our electrophysiological data confirm that differences in spike train properties are also found in the cerebellum and our optogenetic experiments suggest that these spike trains are not merely biomarkers that correlate with the disease state but are sufficient to cause motor impairments. Therefore, cerebellar-targeted DBS may be highly beneficial in normalizing the disease-causing spike train patterns.

A parallel motivation has fueled rodent studies to define the anatomical targets, stimulation parameters, and outcome efficiacy in detail (18, 25, 50–52). Although the exact mechanism(s) of DBS remains unclear (51, 53), there is strong support that at least one target of DBS is the actual neuronal signal itself (which the DBS may modify, enhance, dampen, and perhaps even interfere with the given neural spike defects). Indeed, the ability to alter cerebellar spike activity (54) has driven the investigation of the signal properties (40). Evidently, neurotransmission of the faulty activity patterns is required for the expression of disease behaviors (19). Recent works strongly support the hypothesis that changes in activity (rate, pattern, or both) could instigate a range of movement abnormalities (18, 20, 33, 55, 56). However, the current work defines the individual potential of these altered cerebellar signals to initiate specific motor changes. Dystonia can be reliably associated with irregular activity and tremor with highly rhthmic oscillations in the cerebellar nuclei neurons. Ataxia may be caused by a variety of changes that are different from the dystonia and tremor signatures in the severity of misfiring or proportion of neurons affected. Together, these data unveil a critical role for the cerebellum in triggering disease behaviors, with cauasative signals likely originating locally in its circuitry. Each disease may therefore arise as a result of a change in the balance and representaion of neural signatures.

Methods

Animals: Mice were housed in a Level 3, AALAS-certified vivarium. The Institutional Animal Care and Use Committee (IACUC) of Baylor College of Medicine (BCM) reviewed and approved all experimental procedures that involved mice. We used the following transgenic mouse lines: *L7*^{Cre} (also known as *Pcp2*^{Cre}) (57), *Vgat*^{fl} (JAX:012897) (58), *Ptf1a*^{Cre} (JAX:023329) (59), *Vglut2*^{fl} (JAX:012898) (60), *Pdx1*^{Cre} (JAX:014647) (61), *Car8*$^{wdl/wdl}$ (JAX:004625) (10), *Atxn1*^{154Q} (JAX:005601) (62), *Ank1*^{fl} (JAX:036512) (28), and *Ai32* (*Rosa26*$^{lsl\text{-}ChR2\text{-}eYFP}$, JAX:024109) (63). We included mice from both sexes. We used ear punches from pre-weaned pups for PCR genotyping to identify the different transgenic alleles.

Headplate and craniotomy surgery for electrophysiology recordings: Prior to all recordings, we performed a surgery to attach a headplate over bregma and make a craniotomy over the interposed nucleus. This allowed us to collect stable recordings of cerebellar neuron activity while the mouse was awake and with or without a severe motor phenotype. This surgery was detailed in our previous publication (64). In short, mice were given preemptive analgesics including a subcutaneous injection of buprenorphine and meloxicam. Anesthesia was induced using inhaled isoflurane. During the surgery, the mice were kept on a heating blanket to maintain body temperature. Fur was removed from the surgery site using depilatory cream (Nair) and a small incision in the skin was made over the skull. Next, we used a dental drill to make a ~2 mm diameter craniotomy over the interposed nucleus (6.4 mm posterior and 1.3 mm lateral to Bregma). The craniotomy was surrounded by a round chamber and filled with antibiotic ointment until the day of the recording. The recording chamber was closed with a screw top or silicone cap. We also placed a headplate with a hole over Bregma. A small piece of wire was placed vertically over Bregma to identify this anatomical marker on the day of recording. The recording chamber and headplate were attached to the skull using a combination of C and B Metabond Adhesive Luting Cement (Parkell) and methyl methacrylate dental cement (A-M Systems). Mice were allowed to recover from the surgery for at least three days before we began conducting the *in vivo* electrophysiological recordings.

Standard in vivo electrophysiological recordings in awake mice: We performed *in vivo* electrophysiology recordings according to experimental procedures detailed in our previous publications (20, 64, 65). In brief, we placed mice on a rotating foam wheel and stabilized their heads by screwing the implanted headplates to the recording rig. We removed the antibiotic ointment from the recording chamber and replaced it with sterile physiological saline solution (unless otherwise specified). We measured the coordinates of Bregma to determine the coordinates where the electrode would penetrate the surface of the cerebellum. We used tungsten electrodes (2-8 MΩ, Thomas Recording) attached to a preamplifier head stage (NPI Electronic instruments) for our recordings. The position of the recording electrode was controlled using a motorized micromanipulator (MP-255; Sutter Instrument Co.). Neural signals were amplified and bandpass filtered (0.3-13 kHz) using an ELC-03XS amplifier (NPI Electronics) before being digitized using a CED board. All signals were recorded using Spike2 software (CED). We only included neurons recorded between 2.5 and 3.5 mm from the surface that did not exhibit complex spikes (characteristic for Purkinje cell firing) in our analyses of cerebellar nuclei neuron firing patterns. This paper includes reanalyzed data from previously reported studies (18, 20, 28, 65).

Spike sorting and analyses: We previously showed that recording duration influences the estimation of neural firing parameters (66). Therefore, all parameter estimates in this paper are based on 30 seconds (s)-long recordings. We used Spike2 software to sort out spikes from electrophysiological recordings. Information about spike timing were imported and saved in MATLAB databases using custom written code. We described the spike analyses using twelve parameters investigating the properties of interspike intervals (ISI) within the recording; (1) $firing\ rate = \frac{spikes}{s}$; (2) $mean\ instantaneous\ firing\ rate = mean\ (ISI^{-1})$; (3) $median\ instantaneous\ firing\ rate = median\ (ISI^{-1})$; (4) $CV = \frac{stdev(ISI)}{mean(ISI)}$; (5) $CV2 = mean\left(2 \times \left|\frac{ISI_n - ISI_{n-1}}{ISI_n + ISI_{n-1}}\right|\right)$; (6) $skewness = median\ instantaneous\ firing\ rate - firing\ rate$; (7) $ISI_{25} =$

$\% ISI > 25\, ms$; (8) $ISI_{100} = \% ISI > 100\, ms$; (9) $inter\ burst\ pause = mean\,(ISI > (5 * mean\,(ISI))$; (10) $kurtosis = \% ISI\ at\ mode(ISI)$; (11) $rhythmicity\ index = \frac{a_1}{z} + \frac{b_1}{z} + \frac{a_2}{z} + \frac{b_2}{z} + \cdots$; (12) $oscillation\ peaks = number\ of\ peaks\ "a"$. For the calculation of 11 and 12, we performed an autocorrelation analysis for all spikes in the 30 s recording, calculated the rhythmicity index, and found oscillation peaks as previously described (67, 68). We used a bin width of 5 ms. The first oscillation peak was determined as the highest bin between 10 ms and 1.5 times the mean ISI for a given neuron. The difference between the baseline level and the height of the peak was denoted as a_1, the difference between baseline and the depth of the trough was denoted as b_1, and z was the difference between baseline and the total number of spikes included in the analyses. Each subsequent peak was determined as the highest bin between the delay-time of the previous trough and a_n+a_1+10 ms, where a_n is the time of the previous peak. The first trough was determined as the lowest bin between the first peak (a_1) and a_n + a_1. Peaks and troughs were only accepted if their sum was higher than four times the standard deviation of autocorrelation between 0.96 and 1 s lag-time, or if the peak was higher than baseline plus two times the standard deviation and the trough was lower than baseline minus two times the standard deviation.

Supervised classifier learner: We trained our classifier learner using cerebellar nuclei neuron recordings from mixed background control mice (control), *L7^{Cre};Vgat$^{fl/fl}$* mice (ataxia), *Ptf1a^{Cre};Vglut2$^{fl/fl}$* mice (dystonia), and harmaline-injected mice (tremor). We have previously tested these models and consider them as reliable archetypical models for cerebellar movement disorders (17, 18, 20). For the analyses, we reanalyzed previous recordings (18, 20, 28, 35, 65) in addition to newly acquired ones. We only included recordings with a duration of 30 s or longer and calculated parameter estimates as described above. If recordings were longer than 60 s, we also calculated parameter estimates for the second 30 s period. We randomly assigned the parameter estimates calculated from the first 30 s of the recording to the training or validation data set and, when available, we assigned the parameter estimates from the second 30 s of the recording to the remaining data set. This resulted in a training set comprised of 29 neurons from 9 control mice, 19 neurons from 5 ataxic mice, 19 neurons from 8 dystonic mice, and 21 neurons from 6 tremoring mice. The validation set contained 30 neurons from 9 control mice, 18 neurons from 5 ataxic mice, 17 neurons from 7 dystonic mice, and 18 neurons from 5 tremoring mice.

We used the built-in supervised machine learning, MATLAB Classification Learner APP (The Mathworks Inc, version R2021a) to define spike signature parameter value cutoffs. We imported the parameters describing the spiking activity from an Excel (Microsoft) worksheet. We used “Group” (control, ataxia, dystonia, or tremor) as the “Response Variable” and the 12 parameters described above as the “Predictor Variables.” We trained a “Coarse Tree” with maximum number of splits = 3, split criterion = Gini’s diversity index, and surrogate decision splits = off. We exported the trained model to the workspace to validate the classifier learner. We assigned signature identity to recordings based on the trained classifier tree.

Optopatcher in vivo electrophysiology recordings in awake mice: Optopatcher experiments were performed as previously described (69). We prepared the mice for recording by performing a headplate and craniotomy surgery as described above. The electrophysiology rig and setup were the same as described above with the following differences: We used an optopatcher device (ALA Scientific Instruments Inc) that allows for the placement of a custom-made optical fiber (Thorlabs, #FT200UMT) within a glass recording electrode (Harvard Apparatus, #30-0057). The tip of the optical fiber was placed near the tip of the recording electrode and was illuminated via a 465 nm LED light source (ALA Scientific Instruments Inc). On the day of the recording, we pulled glass electrodes (Sutter Instruments, #P-1000), filled the electrodes with physiological saline, and measured their impedance using an ELC-03XS amplifier (NPI Electronics) before recording. Only electrodes with 2-15 MΩ impedance were used. Light stimulation was triggered using custom Spike2 scripts paired with a CED board (CED). All optopatcher recordings were performed in *L7^{Cre};Ai32* mice that express channelrhodopsin in Purkinje cells. Nuclei

neurons included in our analyses were cell recordings between 2.5-3.5 mm from the surface of the cerebellum and were inhibited by brief light stimulation at 465 nm. After we found and isolated a cell, we slowly ramped up the brightness of this brief stimulation until we found the minimal light power that modulated the spiking activity. This minimal power was then used to stimulate the cell with the various test parameters during the recording session.

Optogenetic light stimulation paradigms for optopatcher recordings and behavioral assays: We used the following stimulation parameters to measure signature-specific responses; ataxia: 50 Hz (10 ms light on/ 10 ms light off) square pulses; dystonia: at least 500 ms of 50 Hz (10 ms light on/ 10 ms light off) square pulses interspersed with at 75% chance of 250 ms pauses in stimulation; tremor: 100 Hz pulses (5 ms light on/ 5 ms light off) overlaid with a 10 Hz sinusoid (50 ms parabolic increase and decrease of light power followed by 50 ms light off).

Bilateral optic fiber implant surgery for in vivo behavioral assays: We implanted mice with optical fibers (ThorLabs, #FT200UMT) targeted bilaterally to the interposed cerebellar nuclei to assess the motor phenotypes that result from our stimulation parameters. We previously described this surgical procedure (Brown et al., 2020). Briefly, the mice were given subcutaneous injections of sustained-release buprenorphine and meloxicam as preemptive analgesics. Anesthesia was induced with 3% isoflurane gas and the anesthetic plane was maintained with 2% isoflurane gas. The mice were placed on a heating blanket and the head was stabilized in a stereotaxic frame (David Kopf Instruments). Fur was removed from the top of the head using depilatory cream (Nair). The surgical site was cleaned using alternating applications of betadine scrub and alcohol. An incision was made in the skin to expose the skull from anterior to bregma to the posterior aspect of the occipital plate. The fascia was removed from the top of the skull and a scalpel was used to etch fine grooves into the top of the skull. A small craniotomy was made in the parietal plate with a dental drill in order to attach a skull screw (00-90 x 1/16 flat point stainless steel machine screw) to anchor the implant to the skull. The skull screw was advanced only until the point that it was stable in the skull and care was taken to ensure it did not contact the brain. The implant sites were determined by measuring 6.4 mm posterior and ±1.5 mm lateral to bregma. Small craniotomies were made at these sites using a dental drill. The base of the fibers were placed on the surface of the cerebellum and were advanced ventrally for 2 mm. A small amount of antibiotic ointment was placed around each fiber to prevent Metabond or dental cement from entering the craniotomy. Metabond was applied over the entire exposed area of skull and around the skull screw and fibers. Two short segments of wire were embedded in the Metabond to allow the experimenter to hold the mouse's head while attaching and removing the fiber patch cables from the implant. Dental cement was placed over the Metabond. The mice were allowed to recover for at least 3 days before any behavioral assessments were made. Subcutaneous injections of meloxicam were provided every 24 h during the recovery period. Eight mice (number of mice, N) were implanted and tested with all three behavioral assays.

Gait analysis: Measurements of gait were made for all mice both before (baseline) and during each stimulation parameter. To do this, the mice were briefly scruffed and then contrasting colored non-toxic paints were applied to the soles of their forepaws and hindpaws (blue paint for forepaws and red paint for hindpaws). The mice were then gently set down on a piece of blank white paper positioned between two parallel plexiglass barriers with a dark enclosed area at the end of the corridor. Adult mice are naturally inclined to walk towards the dark enclosed area, meanwhile depositing paint on the paper with each footstep. The stimulation, if present, was extinguished once the mice entered the enclosed area. The mice were allowed to rest for at least 2 min between each trial. A trial was considered successful if there were at least four hind and forepaw prints for both the left and right feet that were visible, steady (the mouse was neither running or stopping midway through the series of footsteps), and in as straight of a line as possible (the mouse was not actively turning during the trial). Optic patch cables were connected to the implant during every trial (including baseline runs when stimulation was not present). At least two successful trails were collected per stimulation parameter. For analysis, measurements from

two trials of the same type were averaged to determine the values for each mouse. These measurements were stride, the distance from one footprint to the next from the same foot and hind to fore distance, and hind-to-fore distance, the distance from one hindpaw placement from a corresponding forepaw placement on the same side of the body. Three of each measurement were made per footprint and were averaged to determine the measurements per foot, per trial. These trials were then averaged to determine the final measurements for each mouse. A repeated-measures one-way ANOVA with a Tukey multiple comparison adjustment was performed to determine significance. Significance values were indicated as not significant (ns) if $p > 0.05$, * = $p \leq 0.05$. ** = $p \leq 0.01$.

Dystonia rating scale: Mice were placed in a rectangular plexiglass arena in order to phenotypically rate the frequency and severity of dystonic behavior as described previously (Jinnah et al., 2000; Pizoli et al., 2002). The videos were captured to include the animals' behavior before (baseline) and during each stimulation paradigm (ataxia, dystonia, and tremor). Each stimulation period lasted 2 min, during which the mouse was allowed to ambulate freely as well as in response to disturbance by the experimenter. The rating period excluded the first 10 s after stimulation was initiated to avoid including behavior in response to the sudden application of stimulation. Mice were given a score of 0 if no motor abnormalities were identified, 1 if there was abnormal motor behavior that was not obviously dystonic (such as severe tremor), 2 if there was a mild motor phenotype that included dystonic behaviors that may occur only in response to being disturbed by the experimenter or unprovoked (such as brief hyperextension of the limbs or extension of the neck and/or back), 3 if there was moderate severity or frequent unprovoked dystonic behaviors, 4 if there were severe unprovoked dystonic behaviors, and 5 if there were severe unprovoked dystonic behaviors that made goal-directed ambulation extremely difficult or impossible for an extended time. A detailed description of dystonic phenotypes in mice can be found in Brown et al. 2022 (22). Wilcoxon matched-pairs signed rank tests were performed with a post-hoc Holm-Sidak method for p-value adjustment in order to determine significance. Significance values were indicated as not significant (ns) if $p > 0.05$, * = $p \leq 0.05$. ** = $p \leq 0.01$.

Tremor analysis: The amplitude and frequency of tremor before (baseline) and during optogenetic stimulation was measured using a custom-made tremor monitor as previously described (20, 35, 65)The mice were implanted with optical fibers targeted to the interposed nucleus as described above. LED drivers were connected to the implant via optical patch cables and placed above the tremor monitor chamber. The tremor monitor chamber is a clear plexiglass box that is suspended by elastic cords that are connected to each corner of the box. An accelerometer is securely mounted to the bottom of the box to detect the tremor of the mouse within the box. The mice were placed in the chamber and were able to freely ambulate while in the box. They were given 2 min to acclimate to the novel tremor monitor environment before 2 min duration baseline recordings were made. The mice were then stimulated with the ataxia, dystonia, and tremor stimulation parameters for 2 min per stimulation period. At least 2 min were allowed to elapse between stimulation periods. Mice were encouraged to ambulate a similar amount during all recording periods. The output from the tremor monitor was amplified and lowpass filtered at 5 kHz (Brownlee Precision, Model 410) before being digitized by a CED board and analyzed using Spike2 scripts. Tremor monitor recordings were centered on zero and downsampled using the Spike2 interpolate function. A power spectrum analysis with a Hanning window was performed on each recording period. The peak power was calculated as the maximum power between 0 and 30 Hz, which is consistent with the range that we typically observe for physiological and pathological tremor in mice (20). A repeated-measures one-way ANOVA with a Tukey multiple comparison adjustment was performed to determine significance. Significance values were indicated as not significant (ns) if $p > 0.05$, * = $p \leq 0.05$. ** = $p \leq 0.01$.

Histology: After electrophysiology and behavior experimentation, mice were heavily anesthetized with avertin (2,2,2-tribromoethanol, Sigma-Aldrich, St. Louis, MO, USA; #T48402) and transcardially perfused with ice-cold phosphate buffered saline (PBS, 1x) followed by ice-cold 4% paraformaldehyde (PFA). The

implants were removed, and then the brains were dissected out of the skull. The brains were post-fixed in PFA at 4°C for at least 24 hours. They were then cryoprotected via a sucrose gradient, starting at 15% sucrose in PBS followed by 30% sucrose in PBS. The brains were imbedded in Tissue-Tek O.C.T. Compound (Sakura, Torrance, CA, USA), frozen, and then sliced on a cryostat to produce 40 µm thickness sections. The tissue sections were washed in PBS, mounted onto slides, and allowed to dry on the slide for at least 2 hours. The sections were put in a xylene and ethanol series with ~2 min per submersion in the following order: 100% xylene, 100% xylene, 100% ethanol, 100% ethanol, 90% ethanol, 70% ethanol. The sections were then placed in water for ~2 min and then submerged in cresyl violet solution until the stain was sufficiently dark. They were then dehydrated by reversing the series with ~30 s per submersion. Finally, Cytoseal XYL mounting media (Thermo Scientific, Waltham, MA, USA, #22-050-262) and a cover slip were placed on the slides. The slides were allowed to dry in a fume hood before imaging. Photomicrographs were obtained using a Leica DM4000 B LED microscope equipped with a Leica DMC 2900 camera and Leica Application Suite X (LAS X) software. Images were corrected for brightness and contrast using Adobe Photoshop (Adobe Systems, San Jose, CA, USA). Figure panels were made using Adobe Illustrator software.

Acknowledgements
This work was supported by Baylor College of Medicine (BCM), Texas Children's Hospital, The Hamill Foundation, and the National Institutes of Neurological Disorders and Stroke (NINDS) R01NS100874, R01NS119301, and R01NS127435 to RVS. Research reported in this publication was supported by the Eunice Kennedy Shriver National Institute of Child Health & Human Development of the National Institutes of Health under Award Number P50HD103555 for use of the Cell and Tissue Pathogenesis Core and *In Situ* Hybridization Core (the BCM IDDRC). The content is solely the responsibility of the authors and does not necessarily represent the official views of the National Institutes of Health. MEvdH was supported by a postdoctoral award from the Dystonia Medical Research Foundation (DMRF) and by the K99NS130463. A portion of the data were collected when AMB was supported by F31NS101891.

Author contributions
Conceptualization: MEvdH, AMB, RVS. Methodology: MEvdH, AMB, RVS. Software: MEvdH, AMB. Validation: MEvdH, AMB. Data Analyses: MEvdH, AMB, RVS. Investigation: MEvdH, AMB, DJK, RVS. Data curation: MEvdH, AMB, DJK. Writing – Original Draft: MEvdH, AMB, RVS. Writing – Review & Editing: MEvdH, AMB, RVS. Visualization: MEvdH, AMB. Supervision: RVS. Project Administration: MEvdH, AMB. Funding acquisition: MEvdH, AMB, RVS.

Figure 1. Supervised classifier model predicts mouse phenotype based on spike signatures. **A.** Schematic of network changes causing motor impairments in mouse models for ataxia, dystonia, and tremor. Dotted lines indicate lack of neurotransmission. Color-coded lines indicate primary affected cell type. **B**. Example of spike firing rate averaged over previous 50 ms at each occurring spike for the 5 s spike train in **B'**. **B''** 1 s spike train for the duration indicated in the square box in **B'**. **C.** Histograms of instantaneous firing rate (ISI^{-1}) of the full 30 s spike train used in the classification model. **D.** Classifier model based on training data set (control: n = 29 cells, N = 9 mice; ataxia: n = 19, N = 5; dystonia: n = 19, N = 8; tremor: n = 21, N = 6). **E.** Predicted phenotype of mice based on spike properties in validation data set (control: n = 30 cells, N = 9 mice; ataxia: n = 18, N = 5; dystonia: n = 17, N = 9; tremor: n = 18, N = 5). Categories on X-axis indicate the origin of the recorded neurons. **F.** and **G.** Scatterplot of spike train parameters used to classify neural signatures. Colored boxes indicate the predicted phenotype, colors of circles indicate the origin of the recorded neurons.
PC = Purkinje cell; CN = cerebellar nuclei; IO/CF = inferior olive/climbing fiber.

Figure 2. Spike signatures in ataxia models with different etiologies. **A** 5 s example spike trains (and 1 s inset) of representative cerebellar nuclei neurons recorded in each mutant mouse model. Left: example cell from early disease progression (4-month-old) ataxic *Atxn1*$^{154Q/+}$ mouse. Right: example cell from late disease progression (11-month-old) ataxic *L7*^{Cre}*;Ank1*$^{fl/fl}$ mouse. **B**. Histograms of instantaneous firing rate (ISI^{-1}) of the full 30 s spike train of the example cells in **A.** **C**. Proportion of predicted spike signatures in each of the mouse models. **D.** and **E.** Scatterplot of spike train parameters used to classify neural signatures. Colored boxes indicate the predicted phenotype, colors of circles indicate the origin of the recorded neurons. Control: N = 11, n= 55; *Atxn1*$^{154Q/+}$: N = 4, n = 24; *L7*^{Cre}*;Ank1*$^{fl/fl}$: N = 3, n = 14. **C-E.** are based on classifier model in Figure 1D.

Figure 3. Spike signatures in dystonia models with different etiologies. **A** 5 s example spike trains (and 1 s inset) of representative cerebellar nuclei neurons recorded in each mutant mouse model. Left: example cell from mildly dystonic *Pdx1*^{Cre}*;Vglut2*$^{fl/fl}$ mouse. Right: example cell from severely dystonic cerebellum ouabain infusion mouse. **B**. Histograms of instantaneous firing rate (ISI^{-1}) of the full 30 s spike train of the example cells in **A.** **C**. Proportion of predicted spike signatures in each of the mouse models. **D.** and **E.** Scatterplot of spike train parameters used to classify neural signatures. Colored boxes indicate the predicted phenotype, colors of circles indicate the origin of the recorded neurons. Control: N = 6, n= 28; *Pdx1*^{Cre}*;Vglut2*$^{fl/fl}$: N = 4, n = 21; cerebellum ouabain infusion: N = 4, n = 20. **C-E.** are based on classifier model in Figure 1D.

Figure 4. Spike signatures in tremor models with different etiologies. **A** 5 s example spike trains (and 1 s inset) of representative cerebellar nuclei neurons recorded in each mutant mouse model. Left: example cell from *Car8*$^{wdl/wdl}$ mouse with complex phenotype including severe tremor. Right: example cell from *Car8*$^{wdl/wdl}$ mouse with complex phenotype treated with propranolol to treat tremor. **B**. Histograms of instantaneous firing rate (ISI^{-1}) of the full 30 s spike train of the example cells in **A.** **C**. Proportion of predicted spike signatures in each of the mouse models. **D.** and **E.** Scatterplot of spike train parameters used to classify neural signatures. Colored boxes indicate the predicted phenotype, colors of circles indicate the origin of the recorded neurons. Control: N = 4, n= 14; *Car8*$^{wdl/wdl}$: N = 9, n = 19; *Car8*$^{wdl/wdl}$ + propranolol: N = 6, n = 15. **C-E.** are based on classifier model in Figure 1D.

Figure 5. Spike signatures in cerebellar nuclei neurons can be induced by specific stimulation paradigms of Purkinje cells. **A.** Schematic of experimental setup with recordings in awake, head-fixed mice. **B.** Optopatcher recordings of cerebellar nuclei neurons. The opsin is expressed in Purkinje cells (pink) and recordings of nuclei neurons are performed. PC = Purkinje cell; CN = cerebellar nuclei; IO/CF = inferior olive/climbing fiber. **C.** Example validation that light stimulation of inhibitory Purkinje cells (blue bars) inhibits nuclei neurons during light stimulation. The lower trace is a blown-up view of the boxed area in the upper trace. **D.** Example of spike firing rate averaged over previous 50 ms at each occurring spike for the 5 s spike train in **D'**. **D''** 1 s spike train for the duration indicated in the square box in **D'**. Blue bars indicate light stimulation and are specific for ataxia, dystonia, and tremor (see methods for light stimulation parameters). All example traces originate from the same nuclei neuron, indicating that the cell's spike signature can change depending on the light stimulation paradigm. **E.** Histograms of instantaneous firing rate (ISI^{-1}) of the full 30 s spike train, observe the shift in distribution from baseline during the different stimulation paradigms. **F.** Proportion of cells of each predicted spike signature during each of the light stimulations based on classifier model in Figure 1D. Control: n = 11 cells, N = 4 mice; ataxia: n = 9, N = 3; dystonia: n = 7, N = 3; tremor n = 9, N = 4. **G.** and **H.** Scatterplot of spike train parameters used to classify neural signatures. Colored boxes indicate the predicted phenotype, colors of circles indicate the origin of the recorded neurons.

Figure 6. Induced spike signatures elicit distinct cerebellar phenotypes. **A.** Schematic of external view of bilateral optical fiber implant. **B.** Schematic of a coronal section from a mouse cerebellum with bilateral optic fiber implants directed towards the cerebellar nuclei. FN = fastigial nucleus. IN = interposed nucleus. DN = dentate nucleus. **C.** Photomicrograph of a Nissl-stained coronal section from a mouse cerebellum that had been implanted with optic fibers. Arrows = optic fiber tracks. Dotted lines surround the cerebellar nuclei indicated in **B**. Scale = 1 cm. **D.** Schematic of a mouse with bilateral optic fiber implants freely moving in a tremor monitor. **E-K.** Data associated with gait measurements. **E-H.** Example footprints from a single mouse before stimulation (baseline, **E**) and during ataxia (**F**), dystonia (**G**), and tremor stimulation (**H**). Scale = 1 cm. **I-K.** Measurements of gait including the length of the hindpaw stride (**I**), forepaw stride (**J**), and distance between the hind and forepaws (**K**). N = 8. * = $p \leq 0.05$. ** = $p \leq 0.01$. **L**. Example images of phenotypes associated with dystonia. 1 = erect tail. 2 = high stepping. 3 = kinked tail. 4 = hyperextension of the limbs. 5 = splayed toes. **M.** Dystonia rating of mice before stimulation and during stimulation with each paradigm. N = 8. * = $p \leq 0.05$. **N.** Tremor signals detected via tremor monitor from a mouse before and during stimulation with each paradigm. Horizontal scale = 1 sec. Vertical scale = 50 mV. **O.** Population average power spectrums of tremor. Solid line = mean power. Shaded region = SEM. **P.** Peak tremor power of mice before and during stimulation with each paradigm. N = 8. * = $p \leq 0.05$. ** = $p \leq 0.01$. **Q-S.** 2-D comparisons of gait (hind to fore distance), dystonia (rating), and tremor (peak power) measurements from all mice. N = 8. **T.** 3-D plot of data in **Q-S**.

Video 1. Examples of freely moving mouse behavior in a control mouse, an ataxic mouse, a dystonic mouse, and a tremoring mouse.

Video 2. Optogenetically-induced behavioral responses in head-fixed mice. Subtle features of ataxia, dystonia, and tremor can be induced in head-fixed mice by initiating each specific spike signature. In this experiment, the optopatcher recording and stimulation allowed for tracking the inductions of spike signatures in single-units and the subsequent presentation of the disease-associated behaviors. In this video, we show an example of a single trace of multiunit activity recorded from the cerebellar cortex (putative Purkinje cell activity) with the voltage of the trace played as audio in response to all stimulation paradigms and a video of the mouse's behavioral response to each paradigm during the recording.

Video 3. Optogenetically-induced spike signatures result in severe cerebellar phenotypes. Examples of a single freely moving mouse's behavior at baseline and in response to bilateral induction of spike signatures.

Video 4. Optogenetically-induced spike signatures affect gait. Examples of a single mouse's gait within a footprinting corridor at baseline and in response to bilateral induction of spike signatures.

Supplemental Figure 1. Distribution of spike train parameters in control, ataxic, dystonic, and tremor mice. Values and group differences in spike train rate (**A.** firing rate; **B.** mean ISI^{-1}; **C.** median ISI^{-1}), irregularity (**D.** CV; **E.** CV2; **F.** skewness), pauses (**G.** ISI_{25}; **H.** ISI_{100}; **I.** inter burst pause), and rhythmicity (**J.** kurtosis; **K.** rhythmicity index; **L.** oscillation peak number) (see methods for parameter definitions). The coarse classifier model identified the orange highlighted parameters and dotted lines as parameters and threshold values that best differentiated between the groups of cells. Boxplots indicate 25th, 50th, and 75th percentile. Each circle is the parameter value for one neuron in the training set for the coarse classifier model. * = $p<0.05$, ** = $p<0.01$, *** = $p<0.001$, **** = $p<0.0001$. For **A.-K.** differences were tested using one-way ANOVA followed by a Tukey post-hoc analyses. For **L.** differences were tested using a Kolmogorov test followed by a Tukey post-hoc analyses. Control mice = healthy mice; ataxia model = $L7^{Cre/+};Vgat^{fl/fl}$; dystonia model = $Ptf1a^{Cre/+};Vglut2^{fl/fl}$; tremor model = harmaline injection (see also supplemental Table 1).

Supplemental Figure 2. Purkinje cells respond differently to specific optogenetic stimulation paradigms. A. Optopatcher recordings of a Purkinje cell. The opsin is expressed in Purkinje cells (pink). **B.** Example validation that light stimulation (blue bars) excites Purkinje cells. The pink lines indicate climbing fiber induced complex spikes, further confirming that these recordings are from a Purkinje cell. The lower trace is a blown-up view of the boxed area in the upper trace. **C.** Example of spike firing rate averaged over previous 50 ms at each occurring spike for 5 s spike train in **C'**. **C''** 1 s spike train for the duration indicated in the square box in **C'**. Blue bars indicate light stimulation and are specific for ataxia, dystonia, and tremor (see methods for light stimulation parameters). All example traces originate from the same nuclei neuron, indicating that the cells spike signature can change depending on the light stimulation paradigm. PC = Purkinje cell; CN = cerebellar nuclei; IO/CF = inferior olive/climbing fiber.

Supplemental Table 1: Validation of mouse models of motor disorders. Each model used in this manuscript is listed in the table with the type of model that it is, the predominant phenotype reported for the model, motor behaviors that have been quantified relative to control animals (effect direction is noted when difference is statistically significant), and anatomical changes associated with the model. Only congruent and/or undisputed findings in mice are included. Abbreviations used: Purkinje Cell (PC), vesicular GABA transporter (Vgat), immunohistochemistry (IHC), wheat germ agglutinin (WGA), tyrosine hydroxylase (TH), vesicular glutamate transporter 2 (Vglut2), inferior olive (IO), electromyography (EMG), cerebellar nuclei (CN), spinocerebellar ataxia type 1 (SCA1), carbonic anhydrase-related protein 8 (Car8), granule cell (GC), climbing fiber (CF), mossy fiber (MF), lateral hypothalamus (LH), not available (NA).

Mouse Model	Model Type	Predominant Phenotype	Quantified Motor Behavior	Anatomy
L7^{Cre};Vgat$^{fl/fl}$	Cre-loxP constitutive genetic knockout	Ataxia	**<u>Impaired</u>** ↓ **Hind stride:** Footprint analysis ↓ **Latency to fall:** Rotarod ↓ **Tremor amplitude:** Tremor monitor (Brown et al., 2020; White et al., 2014)	↓ **PC Vgat:** IHC and in situ **Abnormal cerebellar zones:** IHC and WGA tracing ↑ **Ectopic TH expression:** IHC (White et al., 2014)
Ptf1a^{Cre};Vglut2$^{fl/fl}$	Cre-loxP constitutive genetic knockout	Dystonia	**<u>Impaired</u>** ↓ **Distance traveled:** Open field ↓ **Latency to fall:** Rotarod ↑ **Tremor amplitude:** Tremor monitor ↑ **Dystonia rating:** Dystonia rating scale ↑ **EMG power:** EMG ↑ **Antagonist muscle co-contraction and over-contraction:** EMG (Brown et al., 2022, 2023; Salazar Leon & Sillitoe, 2023; White & Sillitoe, 2017)	↓ **IO Vgat:** IHC and in situ **Transiently thinner molecular layer:** IHC (Salazar Leon & Sillitoe, 2023; White & Sillitoe, 2017)
Harmaline injection (control genotype)	Intraperitoneal injection (pharmacological)	Tremor	**<u>Impaired</u>** ↑ **Tremor amplitude:** Tremor monitor ↑ **EMG power:** EMG (Brown et al., 2020, 2023)	↑ **CN and IO cFos expression:** IHC (Brown et al., 2020)
Atxn1$^{154Q/+}$	SCA1 genetic knockin	Ataxia	**<u>Impaired</u>** ↓ **Latency to fall:**	↓ **Brain weight** ↑ **Nuclear inclusions:** IHC

			Rotarod ↓ **Distance traveled:** Open field ↑ **Slips** Dowel Assay (Coffin et al., 2023; Fryer et al., 2011; Watase et al., 2002)	↓ **Calbindin immunofluorescence:** IHC **Thinner molecular layer:** IHC ↓ **PC count:** IHC ↑ **Abnormal morphology and degeneration of motor neurons:** H&E ↑ **Reactive astrocytosis:** IHC (Coffin et al., 2023; Fryer et al., 2011; Orengo et al., 2018; Watase et al., 2002)
Pdx1^{Cre};Vglut2$^{fl/fl}$	Cre-loxP constitutive genetic knockout	Dystonia	**<u>Impaired</u>** ↑ **Hind sway:** Footprint analysis ↓ **Latency to fall:** Rotarod ↑ **Dystonia rating:** Dystonia rating scale ↑ **High stepping gait:** Horizontal ladder (Lackey, 2021)	↓ **CF and MF Vglut2:** IHC ↓ **LH Vglut2:** in situ (Lackey, 2021) (Mangieri et al., 2018)
L7^{Cre};Ank1$^{fl/fl}$	Cre-loxP constitutive genetic knockout	Ataxia	**<u>Impaired</u>** ↓ **Hind stride,** ↓ **Hind stance,** ↑ **Hind sway:** Footprint analysis (Stevens et al., 2022)	↓ **PC Ank1:** IHC **PC progressive abnormal morphology and degeneration in anterior and central zones:** IHC **Thinner molecular layer in anterior and central zones:** IHC (Stevens et al., 2022)
Ouabain infusion (control genotype)	Application to the surface of the cerebellum (pharmacological)	Dystonia	**<u>Impaired</u>** ↑ **Dystonia rating:** Dystonia rating scale (Fremont et al., 2014)	NA
Car8$^{wdl/wdl}$	Spontaneous deletion mutation	Ataxia + Dystonia + Tremor	**<u>Impaired</u>** ↓ **Latency to fall:** Rotarod ↓ **Print width,**	↓ **PC Car8:** IHC **Delayed and abnormal cerebellar zones:** IHC and WGA tracing

			↓ **Print area:** CatWalk ↑ **Hind and fore base-width,** ↑ **Hind sway:** Footprint analysis ↑ **Slips** Raised beam ↓ **Ambulatory activity:** Open field ↑ **Tremor amplitude:** Tremor monitor ↑ **Antagonist muscle co-contraction and over-contraction:** EMG **<u>Unimpaired</u>** Righting time, vertical rope climbing, limb clasping (Jiao et al., 2005; Miterko et al., 2019, 2021; White et al., 2016; Zhou et al., 2022)	**Thinner molecular layer:** IHC **Transiently smaller cerebellum:** H&E **Delayed GC proliferation:** IHC **Transiently abnormal PC morphology:** IHC ↑ **Ectopic TH expression:** IHC (Miterko et al., 2019; White et al., 2016)
Car8$^{wdl/wdl}$ + propranolol injection	Spontaneous deletion mutation + intraperitoneal injection (genetic + pharmacological)	Ataxia + Dystonia	**<u>Impaired</u>** ↑ **Hind sway:** Footprint analysis **<u>Unimpaired</u>** Tremor, open field (movement time, movement episodes, ambulatory activity) (Zhou et al., 2022)	NA

Bibliography

1. Flourens P (1841) *Recherches expérimentales sur les propriétés et les fonctions du système nerveux dans les animaux vertébrés* (J.-B. Baillière). 2nd Ed.
2. Holmes G (1917) The symptoms of acute cerebellar injuries due to gunshot injuries. *Brain* 40(4):461–535.
3. Turner WA (1892) Reviews and notices of books. *Brain* 15(2):283–299.
4. Holmes G (1939) The Cerebellum Of Man. *Brain* 62(1):1–30.
5. Balint B, et al. (2018) Dystonia. *Nat Rev Dis Primers* 4(1):25.
6. Falconer DS (1951) Two new mutants, “trembler” and ’reeler’, with neurological actions in the house mouse (Mus musculus L.). *J Genet* 50(2):192–201.
7. Sidman RL, Green MC, Appel SH (1965) *Catalog of the neurological mutants of the mouse* (Harvard University Press, Cambridge, MA and London, England).
8. Guastavino JM, Sotelo C, Damez-Kinselle I (1990) Hot-foot murine mutation: behavioral effects and neuroanatomical alterations. *Brain Res* 523(2):199–210.
9. Rakic P, Sidman RL (1973) Organization of cerebellar cortex secondary to deficit of granule cells in weaver mutant mice. *J Comp Neurol* 152(2):133–161.
10. Jiao Y, et al. (2005) Carbonic anhydrase-related protein VIII deficiency is associated with a distinctive lifelong gait disorder in waddles mice. *Genetics* 171(3):1239–1246.
11. Sidman RL, Lane PW, Dickie MM (1962) Staggerer, a new mutation in the mouse affecting the cerebellum. *Science* 137(3530):610–612.
12. Caddy KW, Sidman RL, Eicher EM (1981) Stumbler, a new mutant mouse with cerebellar disease. *Brain Res* 208(1):251–255.
13. Green MC, Sidman RL (1962) Tottering--a neuromusclar mutation in the mouse. And its linkage with oligosyndacylism. *J Hered* 53:233–237.
14. Phillips RJS (1960) ‘Lurcher’, a new gene in linkage group XI of the house mouse. *J Genet* 57(1):35–42.
15. Snell HD, et al. (2022) Mechanism of stress-induced attacks in an episodic neurologic disorder. *Sci Adv* 8(16):eabh2675.
16. Pan M-K, et al. (2020) Cerebellar oscillations driven by synaptic pruning deficits of cerebellar climbing fibers contribute to tremor pathophysiology. *Sci Transl Med* 12(526).
17. White JJ, et al. (2014) Cerebellar zonal patterning relies on Purkinje cell neurotransmission. *J Neurosci* 34(24):8231–8245.
18. White JJ, Sillitoe RV (2017) Genetic silencing of olivocerebellar synapses causes dystonia-like behaviour in mice. *Nat Commun* 8:14912.
19. Stratton SE, Lorden JF (1991) Effect of harmaline on cells of the inferior olive in the absence of tremor: differential response of genetically dystonic and harmaline-tolerant rats. *Neuroscience* 41(2–3):543–549.
20. Brown AM, et al. (2020) Purkinje cell misfiring generates high-amplitude action tremors that are corrected by cerebellar deep brain stimulation. *Elife* 9.
21. White JJ, et al. (2016) Pathogenesis of severe ataxia and tremor without the typical signs of neurodegeneration. *Neurobiol Dis* 86:86–98.
22. Brown AM, van der Heijden ME, Jinnah HA, Sillitoe RV (2022) Cerebellar dysfunction as a source of dystonic phenotypes in mice. *Cerebellum*.
23. Handforth A (2012) Harmaline tremor: underlying mechanisms in a potential animal model of essential tremor. *Tremor Other Hyperkinet Mov (N Y)* 2.
24. Low AYT, et al. (2018) Precision of discrete and rhythmic forelimb movements requires a distinct

neuronal subpopulation in the interposed anterior nucleus. *Cell Rep* 22(9):2322–2333.
25. Miterko LN, et al. (2021) Neuromodulation of the cerebellum rescues movement in a mouse model of ataxia. *Nat Commun* 12(1):1295.
26. Holt GR, Softky WR, Koch C, Douglas RJ (1996) Comparison of discharge variability in vitro and in vivo in cat visual cortex neurons. *J Neurophysiol* 75(5):1806–1814.
27. Coffin SL, et al. (2023) Disruption of the ATXN1-CIC complex reveals the role of additional nuclear ATXN1 interactors in spinocerebellar ataxia type 1. *Neuron* 111(4):481–492.e8.
28. Stevens SR, et al. (2021) Ankyrin-R regulates fast-spiking interneuron excitability through perineuronal nets and Kv3.1b K+ channels. *Elife* 10.
29. Shakkottai VG, et al. (2017) Current opinions and areas of consensus on the role of the cerebellum in dystonia. *Cerebellum* 16(2):577–594.
30. Shakkottai VG (2014) Physiologic changes associated with cerebellar dystonia. *Cerebellum* 13(5):637–644.
31. Lackey EP (2021) Neural function of Cerebellar inputs in Dystonia-like behavior. . Doctoral dissertation (Baylor College of Medicine).
32. Leon LES, Sillitoe RV (2023) Disrupted sleep in dystonia depends on cerebellar function but not motor symptoms in mice. *BioRxiv*.
33. Fremont R, Calderon DP, Maleki S, Khodakhah K (2014) Abnormal high-frequency burst firing of cerebellar neurons in rapid-onset dystonia-parkinsonism. *J Neurosci* 34(35):11723–11732.
34. Calderon DP, Fremont R, Kraenzlin F, Khodakhah K (2011) The neural substrates of rapid-onset Dystonia-Parkinsonism. *Nat Neurosci* 14(3):357–365.
35. Zhou J, et al. (2022) Propranolol modulates cerebellar circuit activity and reduces tremor. *Cells* 11(23).
36. Pandey S, Sarma N (2016) Tremor in dystonia. *Parkinsonism Relat Disord* 29:3–9.
37. Nibbeling EAR, et al. (2017) Using the shared genetics of dystonia and ataxia to unravel their pathogenesis. *Neurosci Biobehav Rev* 75:22–39.
38. Hagerman PJ, Hagerman RJ (2015) Fragile X-associated tremor/ataxia syndrome. *Ann N Y Acad Sci* 1338(1):58–70.
39. Tara E, Vitenzon A, Hess E, Khodakhah K (2018) Aberrant cerebellar Purkinje cell activity as the cause of motor attacks in a mouse model of episodic ataxia type 2. *Dis Model Mech* 11(9).
40. Slaughter DG, Nashold BS, Somjen GG (1970) Electrical recording with micro- and macroelectrodes from the cerebellum of man. *J Neurosurg* 33(5):524–528.
41. Diniz JM, et al. (2021) Dentate nucleus deep brain stimulation: Technical note of a novel methodology assisted by tractography. *Surg Neurol Int* 12:400.
42. Teixeira MJ, et al. (2015) Deep brain stimulation of the dentate nucleus improves cerebellar ataxia after cerebellar stroke. *Neurology* 85(23):2075–2076.
43. Cury RG, et al. (2021) Safety and outcomes of dentate nucleus deep brain stimulation for cerebellar ataxia. *Cerebellum*.
44. Brown EG, et al. (2020) Cerebellar deep brain stimulation for acquired hemidystonia. *Mov Disord Clin Pract (Hoboken)* 7(2):188–193.
45. Horisawa S, et al. (2021) Case report: deep cerebellar stimulation for tremor and dystonia. *Front Neurol* 12:642904.
46. Paraguay IB, et al. (2021) Dentate nucleus stimulation for essential tremor. *Parkinsonism Relat Disord* 82:121–122.
47. McClelland VM, et al. (2016) Differences in globus pallidus neuronal firing rates and patterns relate to different disease biology in children with dystonia. *J Neurol Neurosurg Psychiatry*

87(9):958–967.
48. Sedov A, et al. (2020) Pallidal Activity in Cervical Dystonia with and Without Head Tremor. *Cerebellum* 19(3):409–418.
49. Tang JKH, et al. (2007) Neuronal firing rates and patterns in the globus pallidus internus of patients with cervical dystonia differ from those with Parkinson's disease. *J Neurophysiol* 98(2):720–729.
50. Cooperrider J, et al. (2014) Chronic deep cerebellar stimulation promotes long-term potentiation, microstructural plasticity, and reorganization of perilesional cortical representation in a rodent model. *J Neurosci* 34(27):9040–9050.
51. Miterko LN, et al. (2019) Consensus paper: experimental neurostimulation of the cerebellum. *Cerebellum* 18(6):1064–1097.
52. Anderson CJ, Anderson DN, Pulst SM, Butson CR, Dorval AD (2020) Neural selectivity, efficiency, and dose equivalence in deep brain stimulation through pulse width tuning and segmented electrodes. *Brain Stimulat* 13(4):1040–1050.
53. Schor JS, et al. (2022) Therapeutic deep brain stimulation disrupts movement-related subthalamic nucleus activity in parkinsonian mice. *Elife* 11.
54. Nashold BS, Slaughter DG (1969) Effects of stimulating or destroying the deep cerebellar regions in man. *J Neurosurg* 31(2):172–186.
55. LeDoux MS, Lorden JF (2002) Abnormal spontaneous and harmaline-stimulated Purkinje cell activity in the awake genetically dystonic rat. *Exp Brain Res* 145(4):457–467.
56. Fremont R, Tewari A, Angueyra C, Khodakhah K (2017) A role for cerebellum in the hereditary dystonia DYT1. *Elife* 6.
57. Lewis PM, Gritli-Linde A, Smeyne R, Kottmann A, McMahon AP (2004) Sonic hedgehog signaling is required for expansion of granule neuron precursors and patterning of the mouse cerebellum. *Dev Biol* 270(2):393–410.
58. Tong Q, Ye C-P, Jones JE, Elmquist JK, Lowell BB (2008) Synaptic release of GABA by AgRP neurons is required for normal regulation of energy balance. *Nat Neurosci* 11(9):998–1000.
59. Nakhai H, et al. (2007) Ptf1a is essential for the differentiation of GABAergic and glycinergic amacrine cells and horizontal cells in the mouse retina. *Development* 134(6):1151–1160.
60. Tong Q, et al. (2007) Synaptic glutamate release by ventromedial hypothalamic neurons is part of the neurocircuitry that prevents hypoglycemia. *Cell Metab* 5(5):383–393.
61. Hingorani SR, et al. (2003) Preinvasive and invasive ductal pancreatic cancer and its early detection in the mouse. *Cancer Cell* 4(6):437–450.
62. Watase K, et al. (2002) A long CAG repeat in the mouse Sca1 locus replicates SCA1 features and reveals the impact of protein solubility on selective neurodegeneration. *Neuron* 34(6):905–919.
63. Madisen L, et al. (2012) A toolbox of Cre-dependent optogenetic transgenic mice for light-induced activation and silencing. *Nat Neurosci* 15(5):793–802.
64. White JJ, et al. (2016) An optimized surgical approach for obtaining stable extracellular single-unit recordings from the cerebellum of head-fixed behaving mice. *J Neurosci Methods* 262:21–31.
65. van der Heijden ME, et al. (2020) Abnormal cerebellar function and tremor in a mouse model for non-manifesting partially penetrant dystonia type 6. *J Physiol (Lond)* 599(7):2037–2054.
66. van der Heijden ME, Brown AM, Sillitoe RV (2022) Influence of data sampling methods on the representation of neural spiking activity in vivo. *iScience* 25(11):105429.
67. Lang EJ, Sugihara I, Llinás R (1997) Differential roles of apamin- and charybdotoxin-sensitive K+ conductances in the generation of inferior olive rhythmicity in vivo. *J Neurosci* 17(8):2825–2838.

68. van der Heijden ME, et al. (2021) Maturation of Purkinje cell firing properties relies on neurogenesis of excitatory neurons. *Elife* 10.
69. van der Heijden ME, Brown AM, Sillitoe RV (2022) in *Measuring Cerebellar Function*, Neuromethods., ed Sillitoe RV (Springer US, New York, NY), pp 47–67.

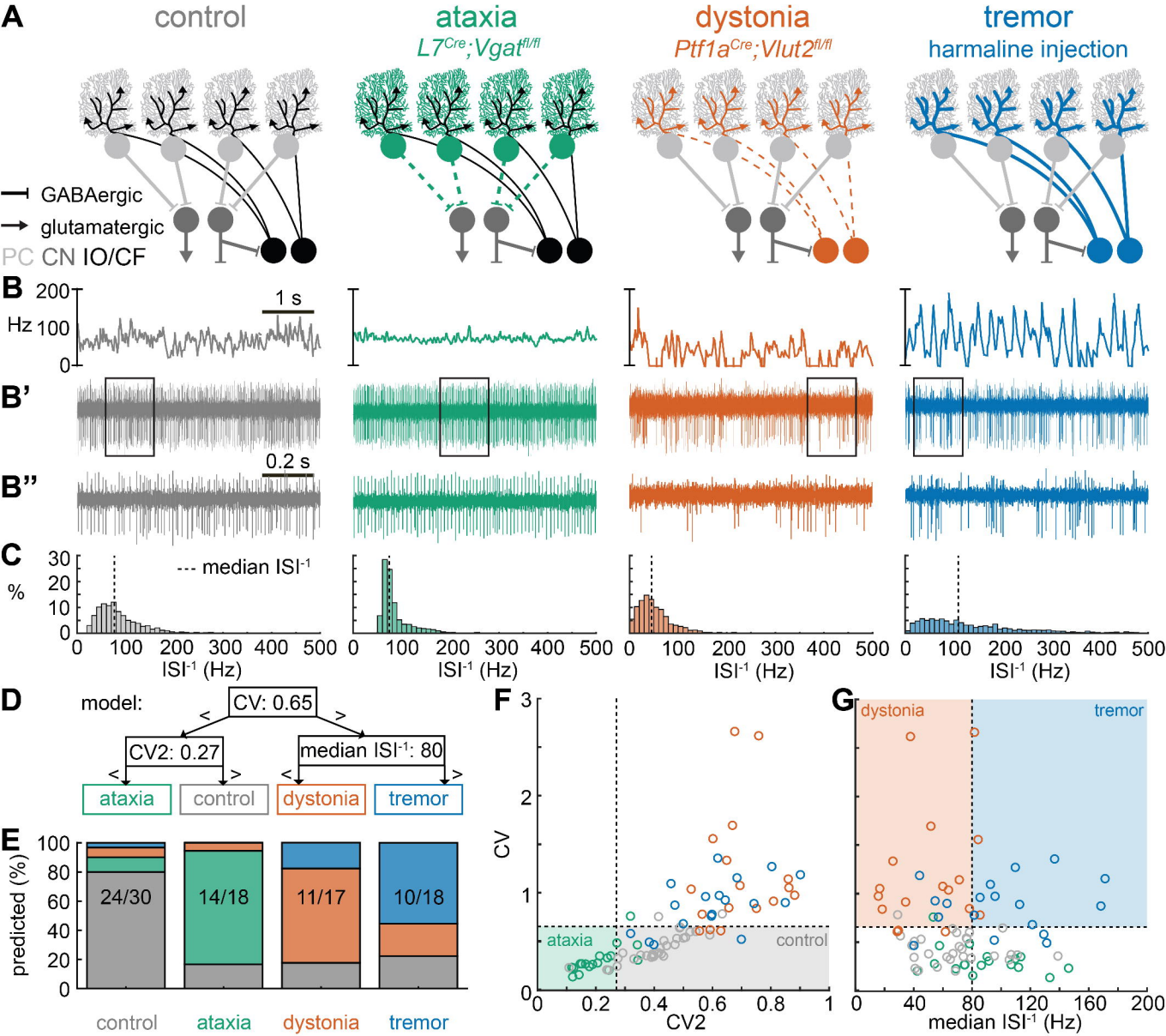
A
control
ataxia
L7Cre;Vgatfl/fl
dystonia
Ptf1aCre;Vlut2fl/fl
tremor
harmaline injection
GABAergic
glutamatergic
PC CN IO/CF
B
200
Hz 100
0
1 s
B'
B''
0.2 s
C
30
20
10
0
%
--- median ISI-1
0 100 200 300 400 500
ISI-1 (Hz)
D
model:
CV: 0.65
CV2: 0.27
median ISI-1: 80
ataxia
control
dystonia
tremor
E
100
80
60
40
20
0
predicted (%)
24/30
14/18
11/17
10/18
control
ataxia
dystonia
tremor
F
3
2
1
0
CV
ataxia
control
0 0.2 0.4 0.6 0.8 1
CV2
G
dystonia
tremor
0 40 80 120 160 200
median ISI-1 (Hz)

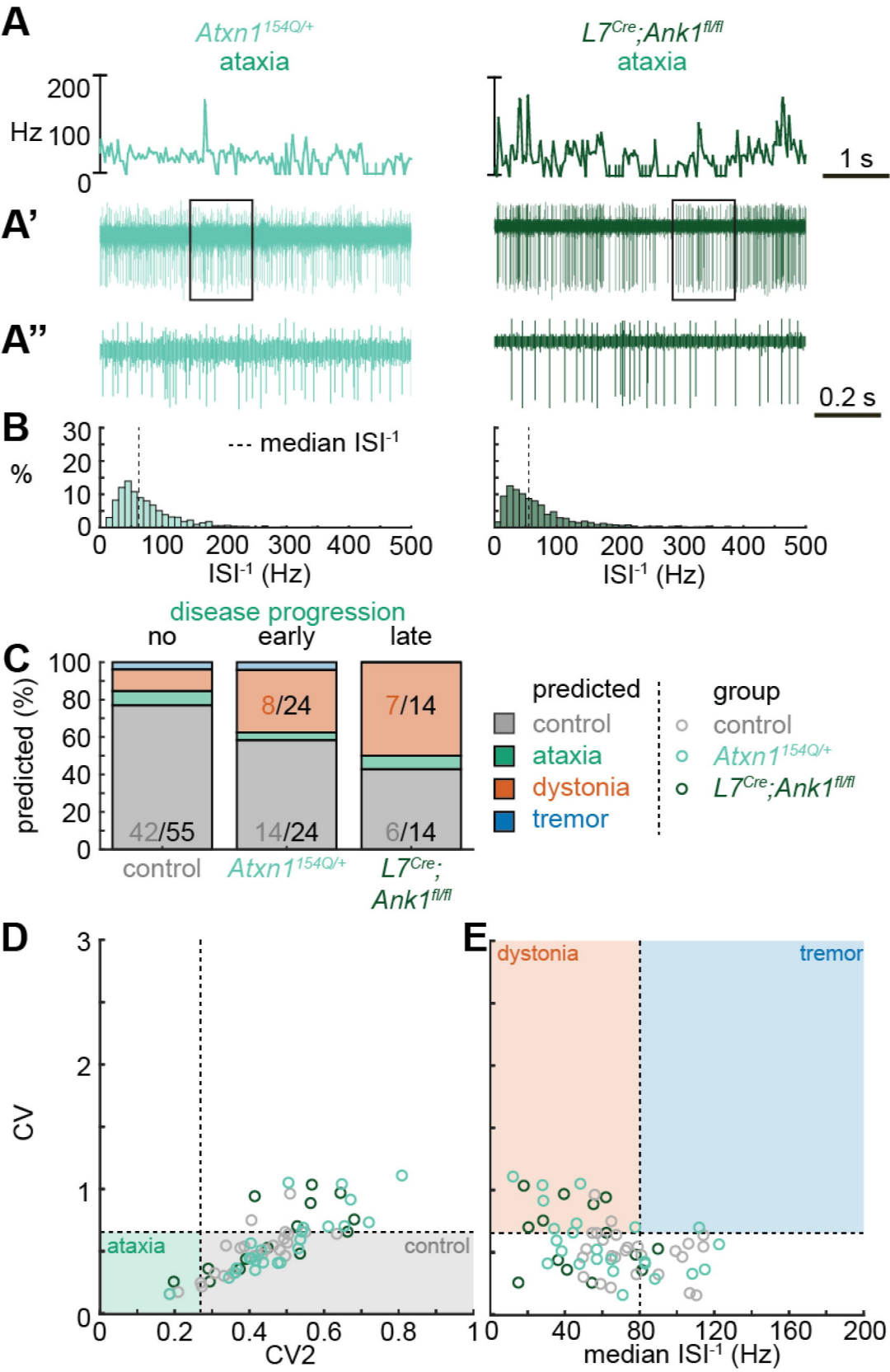
A
Atxn1154Q/+
ataxia
L7Cre;Ank1fl/fl
ataxia
200
Hz 100
0
1 s
A'
A''
0.2 s
B
%
30
20
10
0
--- median ISI-1
0 100 200 300 400 500
ISI-1 (Hz)
0 100 200 300 400 500
ISI-1 (Hz)
disease progression
no
early
late
C
predicted (%)
100
80
60
40
20
0
8/24
7/14
42/55
14/24
6/14
control
Atxn1154Q/+
L7Cre;
Ank1fl/fl
predicted
control
ataxia
dystonia
tremor
group
control
Atxn1154Q/+
L7Cre;Ank1fl/fl
D
CV
3
2
1
0
ataxia
control
0 0.2 0.4 0.6 0.8 1
CV2
E
dystonia
tremor
0 40 80 120 160 200
median ISI-1 (Hz)

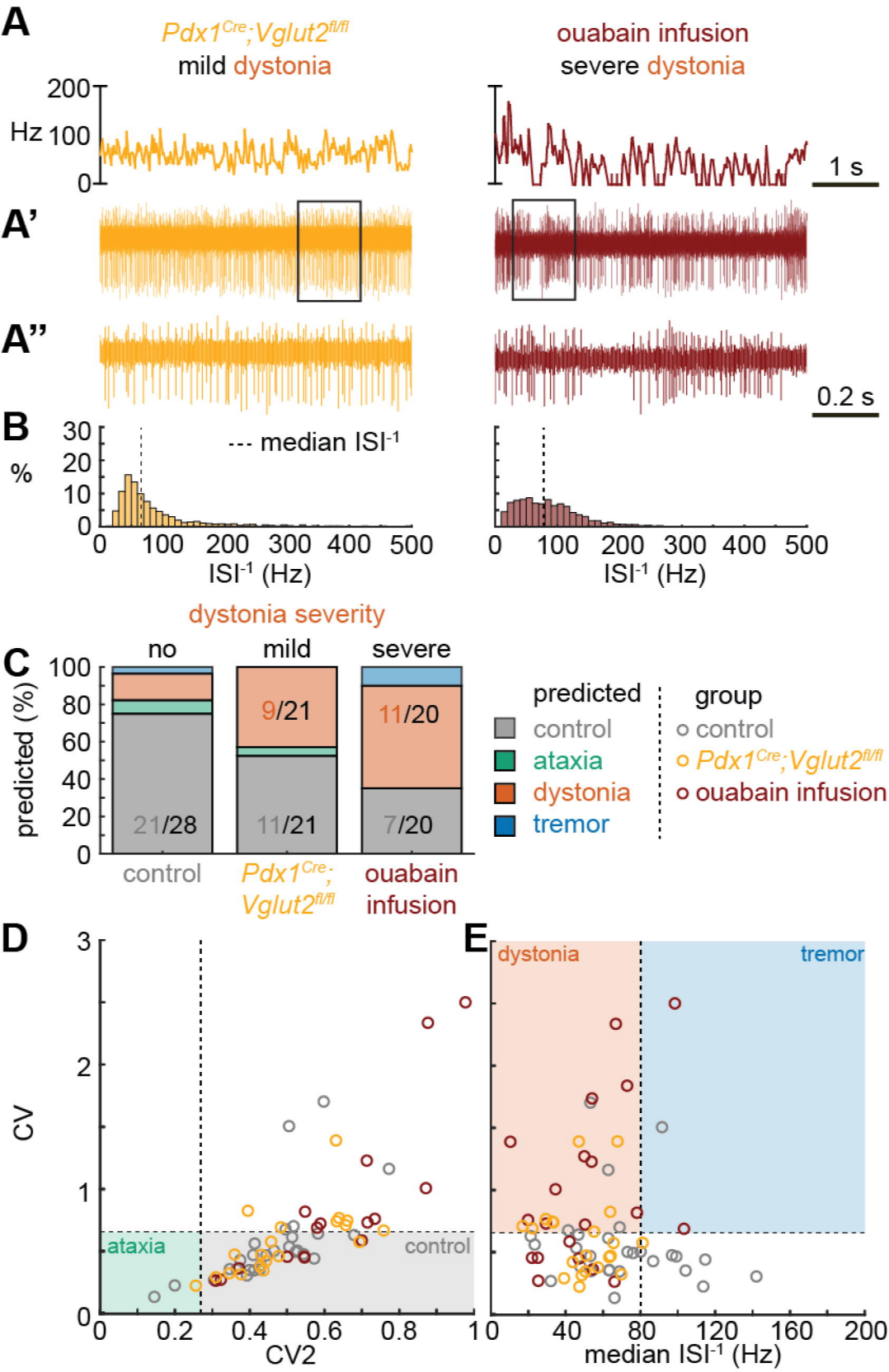
A
Pdx1Cre;Vglut2fl/fl
mild dystonia
ouabain infusion
severe dystonia
200
Hz 100
0
1 s
A'
A''
0.2 s
B
30
20
10
%
0
--- median ISI-1
0 100 200 300 400 500
ISI-1 (Hz)
0 100 200 300 400 500
ISI-1 (Hz)
dystonia severity
C
no
mild
severe
100
80
60
40
20
0
predicted (%)
9/21
11/20
21/28
11/21
7/20
control
Pdx1Cre; Vglut2fl/fl
ouabain infusion
predicted
control
ataxia
dystonia
tremor
group
control
Pdx1Cre;Vglut2fl/fl
ouabain infusion
D
3
2
1
0
CV
ataxia
control
0 0.2 0.4 0.6 0.8 1
CV2
E
dystonia
tremor
0 40 80 120 160 200
median ISI-1 (Hz)

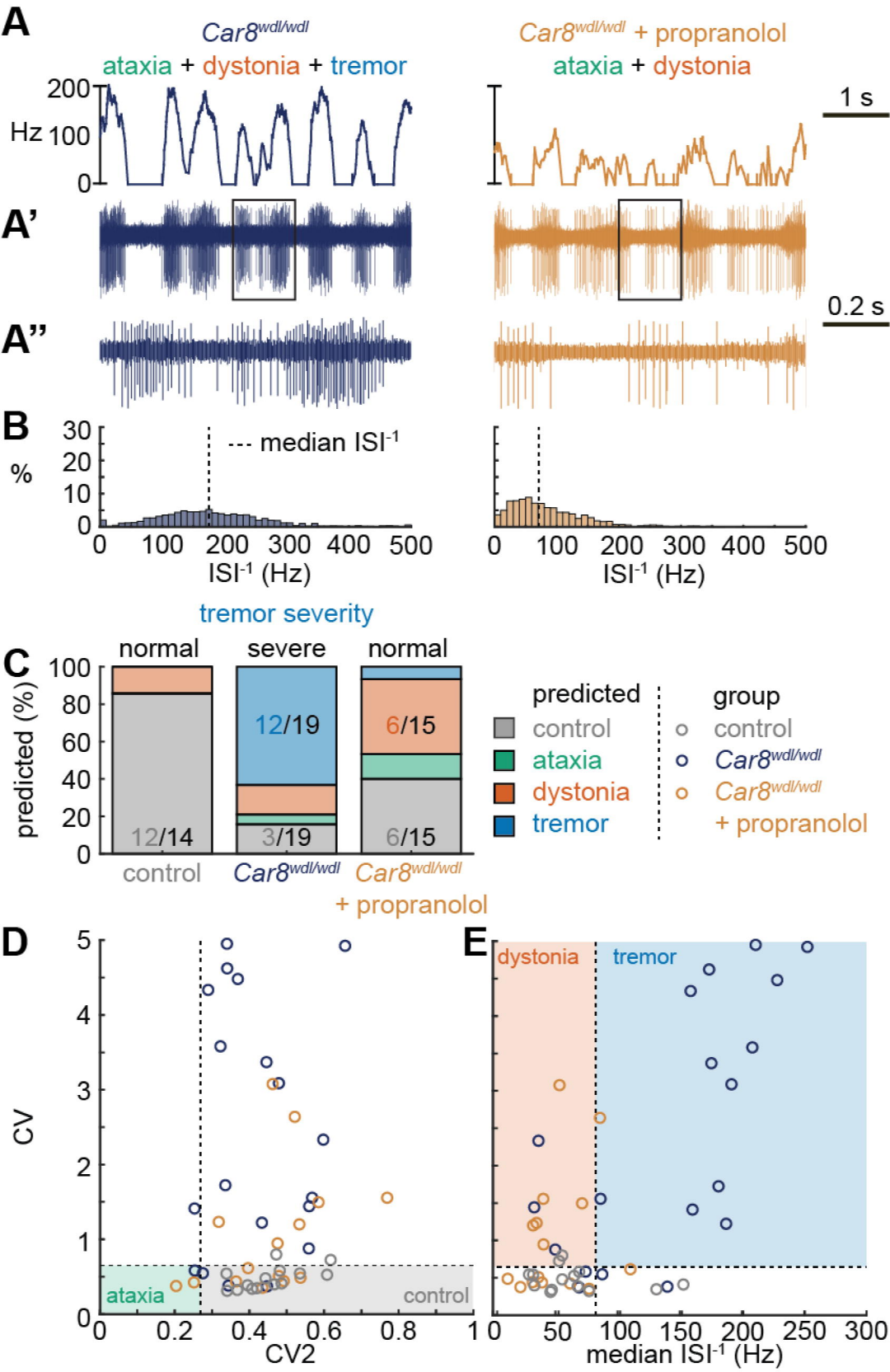
A
Car8wdl/wdl
ataxia + dystonia + tremor
Car8wdl/wdl + propranolol
ataxia + dystonia
200
Hz 100
0
1 s
A'
A''
0.2 s
B
30
20
10
0
%
--- median ISI-1
0 100 200 300 400 500
ISI-1 (Hz)
tremor severity
normal
severe
normal
C
100
80
60
40
20
0
predicted (%)
12/14
12/19
3/19
6/15
6/15
control
Car8wdl/wdl
Car8wdl/wdl
+ propranolol
predicted
control
ataxia
dystonia
tremor
group
control
Car8wdl/wdl
Car8wdl/wdl
+ propranolol
D
5
4
3
2
1
0
CV
ataxia
control
0 0.2 0.4 0.6 0.8 1
CV2
E
dystonia
tremor
0 50 100 150 200 250 300
median ISI-1 (Hz)

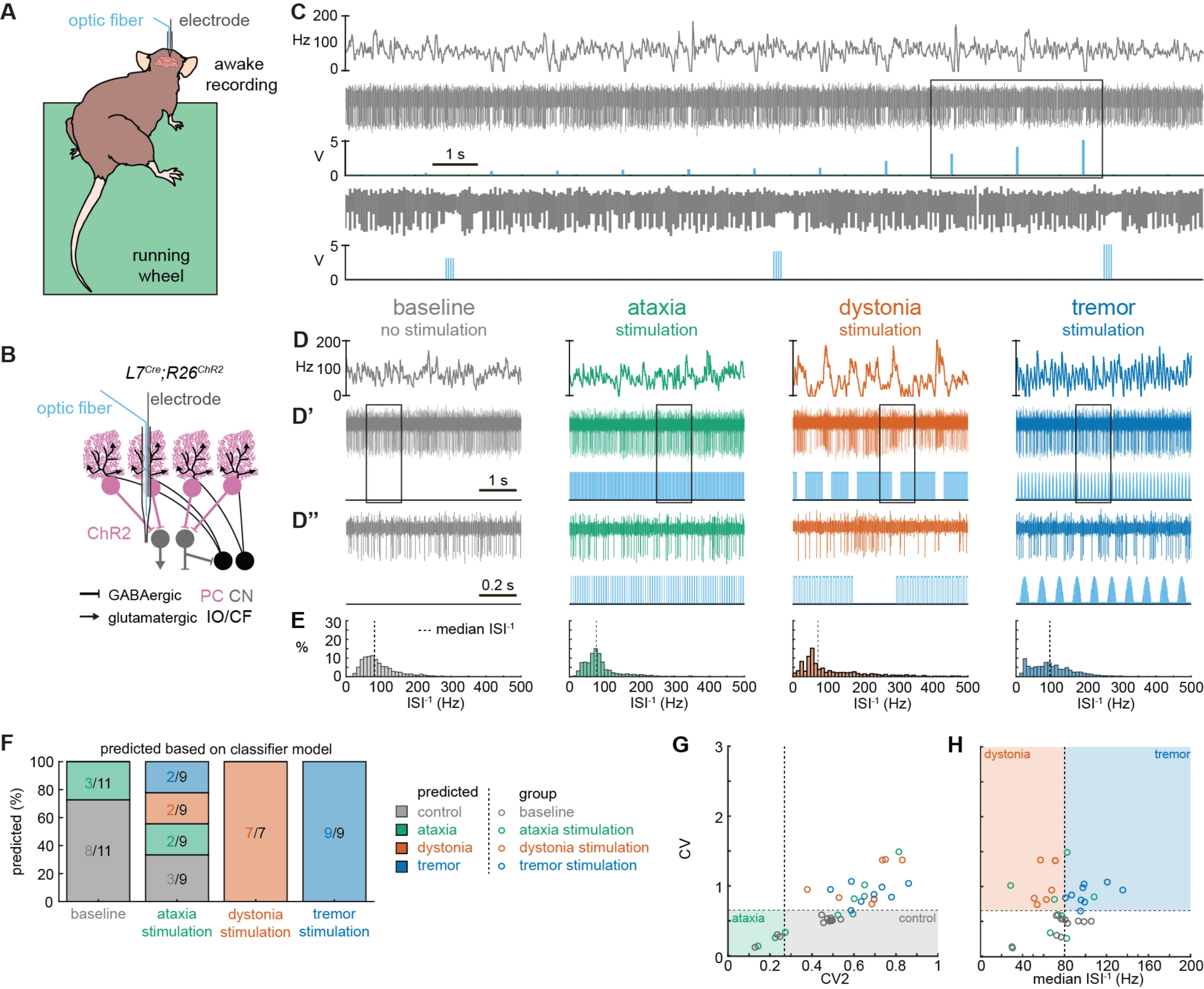
A
optic fiber
electrode
awake recording
running wheel
B
L7Cre;R26ChR2
optic fiber
electrode
ChR2
GABAergic
glutamatergic
PC CN
IO/CF
C
200
Hz 100
0
5
V
0
1 s
5
V
0
D
200
Hz 100
0
D'
1 s
D''
0.2 s
E
30
20
10
0
%
--- median ISI-1
0 100 200 300 400 500
ISI-1 (Hz)
baseline
no stimulation
ataxia
stimulation
dystonia
stimulation
tremor
stimulation
F
predicted based on classifier model
predicted (%)
100
80
60
40
20
0
3/11
8/11
2/9
2/9
2/9
3/9
7/7
9/9
baseline
ataxia stimulation
dystonia stimulation
tremor stimulation
predicted
control
ataxia
dystonia
tremor
group
baseline
ataxia stimulation
dystonia stimulation
tremor stimulation
G
CV
3
2
1
0
ataxia
control
0 0.2 0.4 0.6 0.8 1
CV2
H
dystonia
tremor
0 40 80 120 160 200
median ISI-1 (Hz)

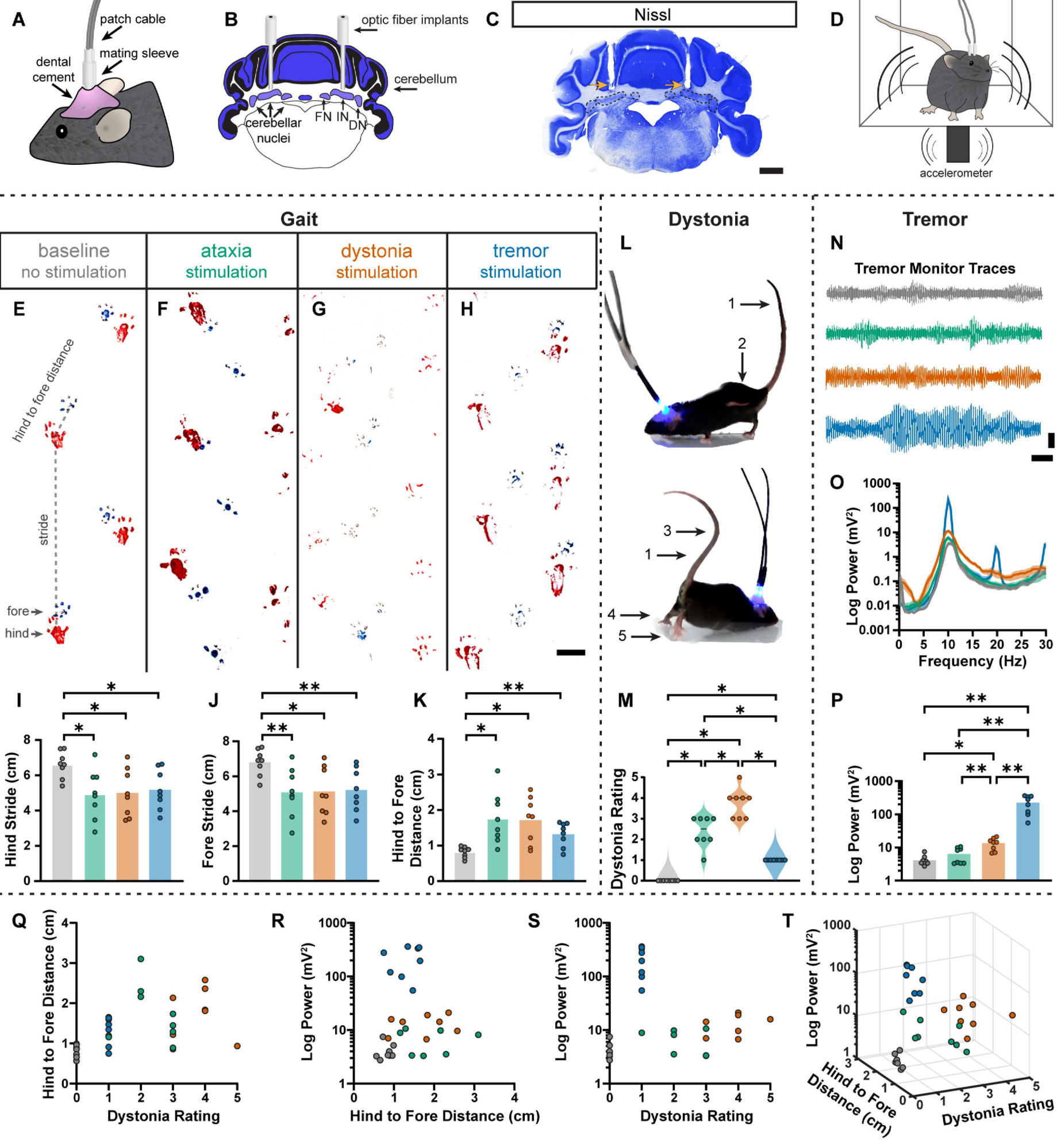
A
patch cable
mating sleeve
dental cement
B
optic fiber implants
cerebellum
cerebellar nuclei
FN
IN
DN
C
Nissl
D
accelerometer
Gait
baseline no stimulation
ataxia stimulation
dystonia stimulation
tremor stimulation
E
F
G
H
hind to fore distance
stride
fore
hind
Dystonia
L
1
2
3
1
4
5
Tremor
N
Tremor Monitor Traces
O
Log Power (mV²)
Frequency (Hz)
I
Hind Stride (cm)
J
Fore Stride (cm)
K
Hind to Fore Distance (cm)
M
Dystonia Rating
P
Log Power (mV²)
Q
Hind to Fore Distance (cm)
Dystonia Rating
R
Log Power (mV²)
Hind to Fore Distance (cm)
S
Log Power (mV²)
Dystonia Rating
T
Log Power (mV²)
Hind to Fore Distance (cm)
Dystonia Rating